A Lagrangian coherent eddy atlas for biogeochemical applications in the North Pacific Subtropical Gyre

Alexandra E. Jones-Kellett[1,2] and Michael J. Follows[1]

[1]Department of Earth, Atmospheric and Planetary Sciences, Massachusetts Institute of Technology, Cambridge, MA, USA
[2]Biology Department, Woods Hole Oceanographic Institution, Woods Hole, MA, USA
Correspondence: Alexandra E. Jones-Kellett (jonesae@mit.edu)

Abstract. Mesoscale eddies modify the vertical structure of the resource environment and affect the horizontal dispersal and mixing of phytoplankton populations. It is useful to characterize the lateral dispersal and trapping properties of eddies for their biogeochemical interpretation. We employ a Lagrangian approach, which provides metrics of material coherence, to identify and track eddies over two decades of remote sensing observations in an intensely studied region of the North Pacific Subtropical Gyre. Emphasizing biogeochemical applications, we use backward-in-time Lagrangian trajectories to compute the coherency of the recent past, synchronize the analysis with ocean color products, and provide a high temporally resolved atlas of coherent eddy boundaries (Jones-Kellett, 2023a, doi.org/10.5281/zenodo.8139149). We compare Lagrangian coherent and Sea Level Anomaly eddy atlases, finding similar variations in temporal and spatial distributions. However, coherent eddies have a more mechanistic relationship between size and longevity and form distinct regional regimes based on polarity. While 65% of tracked Sea Level Anomaly eddies are classified as coherent at some point in their lifetime, only 54% contain a Lagrangian coherent structure at any given time. We illustrate the potential of the coherent eddy atlas for biogeochemical applications by examining the relationship between bloom development and eddy evolution in a case study of a Hawaiian Lee cyclone.

1 Introduction

Mesoscale eddies are ephemeral, highly energetic features with horizontal scales of tens to hundreds of kilometers. They are typically generated by baroclinic instabilities, where the available potential energy of sloped density surfaces is converted into kinetic energy (reviewed by Ferrari and Wunsch, 2009). The mesoscale circulations are in approximate geostrophic balance in the horizontal and hydrostatic balance in the vertical. While small relative to major ocean gyres and current systems, eddies are extremely abundant and can propagate for weeks to months. Their associated vertical and submesoscale motions are known to influence local biogeochemistry, while their recirculating horizontal flows can be important for the retention and redistribution of marine tracers (reviewed by Mahadevan, 2016; McGillicuddy Jr, 2016; Lévy et al., 2018). These impacts on phytoplankton populations, manifested as the pigment chlorophyll-*a* (chl-*a*), can be observed from space. Disentangling the influence of biological processes and physical transport is challenging because mesoscale eddies are not necessarily coherent from a Lagrangian perspective. Recently developed methods for identifying Lagrangian coherent eddy boundaries provide an opportunity to systematically evaluate eddy trapping and tease apart these influences.

In this study, we describe a methodology developed to track Lagrangian coherent structures en masse and present an atlas of two decades of mesoscale activity in the North Pacific Subtropical Gyre (NPSG). First, we briefly review the use of remote sensing to identify mesoscale eddies and their biological signatures. In Section 2, we describe the algorithms employed to build the coherent eddy atlas. To this end, we synchronize the physical analysis to match the availability of remotely sensed ocean color products, use a backward-in-time Lagrangian trajectory analysis, and track features through time to examine eddy evolution. In Section 3, we show key regional features of the eddy atlas, compare Eulerian and Lagrangian eddy characteristics, and present a case study following a localized chl-*a* bloom in a Hawaiian Lee cyclone. Finally, in Section 4, we end with a discussion of the results, analyses, and potential applications of the eddy atlas.

1.1 Mesoscale features in remotely sensed chlorophyll-*a*

The first ocean color observing satellite technology produced images from space that showed evidence of the control of mesoscale eddies on plankton patchiness (Gower et al., 1980). Since the 1990s, there has been continuous, global-scale remote sensing of surface chl-*a*. Simultaneous remote sensing of the physical environment provides an opportunity to identify patterns in the biogeochemical signatures of mesoscale circulations. There are several mechanisms by which mesoscale eddies can alter concentrations of chl-*a* including stirring, eddy-wind interaction, eddy pumping, and eddy trapping (reviewed by McGillicuddy Jr, 2016). The latter two are thought to enhance "monopole" chl-*a* anomalies, where elevated or depressed levels of chl-*a* are located in the core of an eddy. Satellite observations have revealed chl-*a* monopoles in eddies shed from the Gulf Stream and other western boundary currents (Waite et al., 2007; Gaube et al., 2013, 2014; He et al., 2022), the Agulhas rings (Lehahn et al., 2011; Villar et al., 2015), the South (Chelton et al., 2011a) and North (Calil and Richards, 2010; Guo et al., 2017; He et al., 2022) Pacific Ocean, the South Indian Ocean (Gaube et al., 2014), and the Southern Ocean (Dawson et al., 2018; Frenger et al., 2018).

1.2 Eddy detection from satellite altimetry

Satellite altimeters measure the surface Sea Level Anomaly (SLA) from which the geostrophic flow is calculated by assuming a balance between the Coriolis force and the horizontal pressure gradient. Decades of these measurements from the Topex/Poseidon-ERS missions, Jason-Envisat, and more have enabled the identification and characterization of eddies at the global scale. To determine eddy boundaries from satellite observations, early studies employed the Okubo-Weiss (OW) parameter (Okubo, 1970; Weiss, 1991) by demarking boundaries where the local vorticity dominates over the strain, calculated from the geostrophic velocity field (e.g., Isern-Fontanet et al., 2003; Chelton et al., 2007) (see Appendix A). However, this method has high susceptibility to noise in the altimeter data, and thresholds to define boundaries are locally dependent, making it less ideal for global or large-scale eddy identification.

Chelton et al. (2011b) identified eddies globally by defining boundaries as closed contours surrounding local SLA extrema. They found that eddies identified directly from the SLA are nearly all nonlinear, meaning the rotational fluid speed is greater than the translation speed. This characteristic distinguishes mesoscale eddies from Rossby waves, where a high ratio of the rotational to translation speeds enables eddies to trap fluid (Flierl, 1981). When applied to SLA eddies, nonlinearity is an

Eulerian (frozen-in-time) assessment that is dependent on the frame of reference. Yet, the boundaries of a materially invariant vortex must be frame-invariant (i.e., "objective"; reviewed by Haller, 2015). An important distinction must be made that an SLA or OW eddy boundary may contain a trapping structure, but the Eulerian contour itself does not distinguish between fluid that is trapped and fluid that is actively mixing with surrounding waters.

Eddy boundaries derived from the SLA or with the OW parameter clearly fail tests of material invariance (e.g., Beron-Vera et al., 2013; Wang et al., 2015; Beron-Vera et al., 2019; Katsanoulis et al., 2020; Denes et al., 2022). And yet, many studies continue to assume that Eulerian eddy boundaries are coherent. To make such an assumption, Lagrangian coherence metrics are needed. However, Lagrangian methods are computationally expensive and rarely invoked for biophysical interpretations, with a few exceptions. A recent study found that Lagrangian coherent eddies favor diatom growth in the oligotrophic Mediterranean Sea (Hernández-Carrasco et al., 2023). There is also a history of investigation of the finite size and time Lyapunov exponents (FSLE/FTLE) and phytoplankton blooms. The FSLE and FTLE are Lagrangian coherent structure metrics that highlight stretching regions of the flow, including fronts and unstable manifolds (Pierrehumbert and Yang, 1992; Artale et al., 1997; Aurell et al., 1997). Case studies have identified FSLE (Lehahn et al., 2011, 2014; Calil and Richards, 2010; Guidi et al., 2012) or FTLE (Liu et al., 2018) streaks that surround chl-*a* anomalies at eddy cores. They show that Lagrangian coherent structures clearly shape the spatiotemporal chl-*a* patterns at the ocean surface. However, the FSLE and FTLE metrics alone are not appropriate tools to investigate eddy retention en masse because they simultaneously identify fronts and filaments that are not associated with eddies.

Haller et al. (2016) introduced the Lagrangian Averaged Vorticity Deviation (LAVD), a robust, observer-independent method that monitors the vorticity of fluid parcels to detect Rotationally Coherent Lagrangian Vortices (RCLVs; see Section 2.4). These features are ubiquitous in satellite altimetry observations (Abernathey and Haller, 2018; Rousselet et al., 2018; Andrade-Canto et al., 2020; Encinas-Bartos et al., 2022; Liu et al., 2022; Tian et al., 2022; Xia et al., 2022b, a; Liu and Abernathey, 2023). While many SLA-identified eddy boundaries overlap with RCLVs, there are also independent cases of each (Liu et al., 2019). This is further evidence that, from a Lagrangian perspective, some Eulerian eddies cannot be considered coherent for some or possibly all of their lifetime.

To interpret biogeochemical developments in eddies, it is useful to study eddy evolution by tracking features through time and space in a manner similar to SLA eddy atlases (e.g. Chelton et al., 2011b; Mason et al., 2014; Faghmous et al., 2015). To the best of our knowledge, an equivalent RCLV atlas does not exist. Most previous works identify snapshots of RCLV boundaries in bulk at fixed intervals without tracking equivalent features between the intervals. Evaluations of RCLV evolution have only been performed for case studies and over limited domains. For example, Vortmeyer-Kley et al. (2019) tracked short-lived RCLVs in a simulation of the Baltic Sea, Xia et al. (2022a) examined the details of Lagrangian coherency in Agulhas ring evolution, and others followed RCLVs to understand transport in the Caribbean Sea and the Gulf of Mexico (Ntaganou et al., 2023; Andrade-Canto et al., 2020, 2022). Nevertheless, the aforementioned literature does not present methodologies that are well suited for systematically tracking the evolution of a large number of RCLVs, as is characteristic of an eddy atlas.

Liu and Abernathey (2023) identified RCLVs globally every month from satellite altimetry observations. However, phytoplankton populations grow on timescales of the order of days, and acclimation of pigments can be even faster. Thus a higher

temporal resolution mapping of eddy coherency will be valuable when interpreting biophysical interactions in eddies. Further-more, previous work identified RCLVs with forward-in-time Lagrangian trajectories, but biogeochemical states are a function

95   of the physical environment in the recent past, rather than the future. The objective of this study is to present and evaluate a publicly available RCLV atlas product that is particularly useful for applications to characterize the biogeochemical response to eddy trapping. We used backward-in-time Lagrangian simulations to identify RCLVs every 8 days from 2000-2019. We focused on the NPSG region that encompasses the Hawai'i Ocean Time-Series site at Station ALOHA (Karl and Church, 2019) and the locations of other major biogeochemical sampling campaigns that targeted mesoscale features (Falkowski et al., 1991;

100   Seki et al., 2001; Vaillancourt et al., 2003; Benitez-Nelson et al., 2007; Benitez-Nelson and McGillicuddy Jr, 2008; Zhang et al., 2021; Barone et al., 2022). The atlas provides a resource for retrospective analysis of in situ and remote observations and for contextual planning of future expeditions.

2   Materials and methods

2.1   Satellite data

105   Daily Level 4 satellite geostrophic current data from 2000-2019 were obtained from the $1/4°$ Version 008_047 gridded global ocean dataset distributed by CMEMS. This product uses the DUACS multi-mission altimeter data processing system, which combines data from all available altimetry satellites. The SLA is computed with respect to a 20-year mean, and geostrophic currents are derived from the SLA. We restricted the spatial domain of our analysis to 15-30°N and 180-230°W. This encompasses the eastern NPSG, excluding the ultra-oligotrophic waters to the west, the transition zone to the north (Glover et al.,

110   1994), and the equatorial currents to the south.

For the case study in Section 3.4, 8-day average satellite chl-*a* data were obtained for 2010 from Version 6.0 of the Ocean Color Climate Change Initiative (OC-CCI) project. The product merges multiple ocean color sensor products (MERIS, Sea-WiFS, MODIS-Aqua, and VIIRS) for improved coverage, with a nominal spatial resolution of $4\ km$ at the equator (Sathyen-dranath et al., 2019).

115   ### 2.2   Eulerian Sea Level Anomaly eddies

We used the OceanEddies MATLAB software to detect eddies from satellite SLA (Faghmous et al., 2015). The algorithm identifies an eddy boundary as the outermost closed contour containing a single SLA extremum. We required SLA contours to contain at least 12 grid cells to account for noise in the data and prevent spurious detection of small features. As a result, the smallest SLA eddy area in the dataset is $8,048\ km^2$, which has a radius of approximately $50\ km$. This is consistent

120   with the Rossby radius of deformation in the region of interest (Chelton et al., 1998). Eddies were detected at a daily frequency concurrent with the temporal resolution of the satellite SLA product. To account for noise in the SLA and to prevent prematurely "killing" an eddy, we set the eddy disappearance parameter to three days. For the subsequent analysis, we reduced the temporal resolution of the SLA product to an 8-day frequency to align with the RCLV dataset (described in Section 2.4). We also required
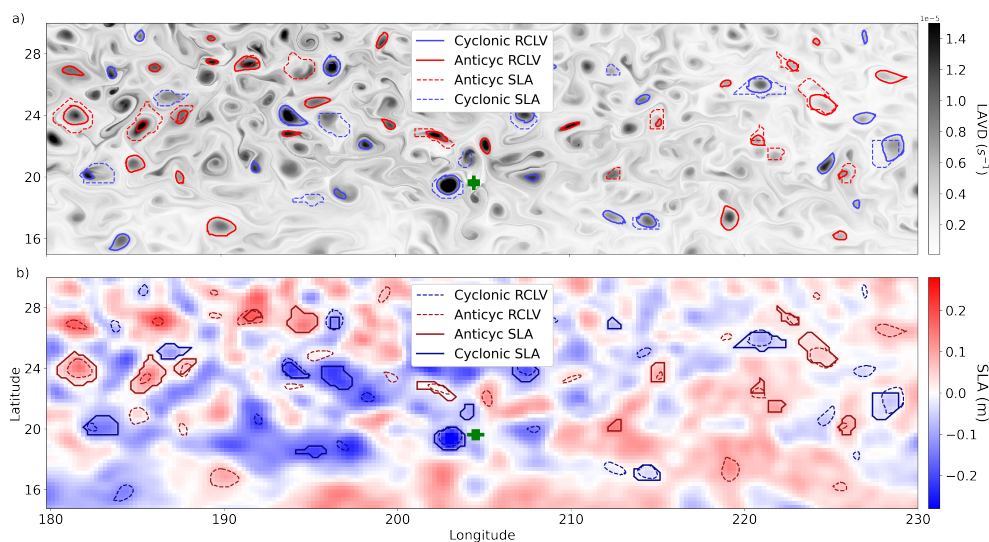
Figure 1. (a) 32-day backward-in-time LAVD field calculated from Lagrangian particles initialized on 23 April 2010. RCLV boundaries are plotted with solid lines. For comparison, the boundaries of SLA eddies that are at least 32 days old are plotted with dotted lines. (b) The SLA field on 23 April 2010.

eddies to have a minimum lifetime of 32 days and removed eddy contours younger than 32 days from the analysis, again to align with the RCLV dataset. Figure 1(b) illustrates an instantaneous satellite SLA field and the corresponding eddy features.

2.3 Lagrangian particle simulations

We conducted Lagrangian particle simulations by implementing a 4th-order Runge-Kutta advection scheme using Ocean-Parcels version 2.2.2, an open-source Python software (Delandmeter and van Sebille, 2019). Particle position (x,y) was calculated from the geostrophic velocity (u,v), such that

$$\frac{\delta x}{\delta t} = u, \frac{\delta y}{\delta t} = v \qquad (1)$$

When seeding the spatial domain with a field of Lagrangian particles, the initial particle spacing must be smaller than the velocity grid size in order to accurately identify RCLVs (Abernathey and Haller, 2018). Accordingly, particles were initialized in an 8×8 grid within each $1/4°$ cell of the velocity grid, resulting in a particle initialization resolution of $1/32°$. This amounted to 768,000 Lagrangian particles in each simulation. We created a custom Kernel within OceanParcels to calculate the relative vorticity (ζ) along the trajectories, where

$$\zeta = \frac{\partial v}{\partial x} - \frac{\partial u}{\partial y} \qquad (2)$$

Particle location and relative vorticity were calculated every 20 minutes. This timestep was selected based on sensitivity tests of particle trajectory convergence. To reduce storage size, the data were output every six hours. We performed sensitivity tests to ensure that this did not reduce the quality of the LAVD field and the RCLV boundary detection. Lagrangian simulations were run backward in time for 32 days to describe the history of fluid parcels. RCLVs derived from backward simulations are coherent over the simulation time interval but need not maintain coherency into the future. The 32-day timescale was chosen to measure coherent features analogous to those in preceding literature (e.g., 30-day RCLVs detected by Abernathey and Haller (2018) and Liu and Abernathey (2023)) and to conveniently align with 8-day ocean color products.

Most previous RCLV studies ran Lagrangian simulations on temporally non-overlapping data (Abernathey and Haller, 2018; Liu et al., 2019; Sinha et al., 2019; Zhang et al., 2020; Tian et al., 2022; Xia et al., 2022b), meaning that subsequent simulations were initialized when the previous ended. This is less computationally expensive than running overlapping simulations, but they do not capture the evolution of the boundaries of a coherent structure at a high resolution. One could track particles between two non-overlapping simulations to interpolate RCLV boundaries, but this would prevent the structure from growing or shrinking for the timescale of the simulations (i.e., 32 days, in our case). Instead, we re-initialized the Lagrangian particles every 8 days to capture boundary evolution at a high resolution. We intentionally aligned the dates of initialization with the 8-day average OC-CCI ocean color products. This amounted to 920, 32-day simulations (3.7 Gb each, 3.4 Tb total) for the 20-year domain and 706,560,000 particle trajectories.

2.4 RCLV atlas

The code used to perform the Lagrangian simulations on CMEMS geostrophic velocity data with OceanParcels and to create the RCLV dataset presented here is available at github.com/lexi-jones/RCLVatlas. Additionally, the 20-year NPSG dataset is distributed by Simons CMAP at simonscmap.com/catalog/datasets/RCLV_atlas.

2.4.1 Boundary detection

We used the LAVD method to identify coherent eddies due to its objectivity, computational efficiency, and mathematical foundation describing material rotation (Haller et al., 2016). The LAVD is a measure of local rotation experienced by a Lagrangian particle integrated over a time interval of interest. For a given fluid element $\mathbf{p}$,

$$LAVD_{t_0}^{t_1}(\mathbf{p}) = \frac{1}{t_1 - t_0} \int_{t_0}^{t_1} |\zeta(\boldsymbol{X}(\mathbf{p},\tau);\tau) - \overline{\zeta(\tau)}| d\tau \tag{3}$$

where $\boldsymbol{X}$ is a Lagrangian trajectory such that $\boldsymbol{X}(\mathbf{p},t)$ is the fluid element's position in space at time t, $\zeta(\boldsymbol{X}(\mathbf{p},t);t)$ is the relative vorticity of the fluid element at time t, $\overline{\zeta(t)}$ is the average relative vorticity across the spatial domain at time t, and $[t_0, t_1]$ is the temporal domain of the Lagrangian simulation. A Lagrangian particle with high LAVD experiences high magnitude relative vorticity along its trajectory over the period of interest. An RCLV is defined as a set of fluid elements that rotate around an eddy core in a manner analogous to rigid-body rotation (Haller et al., 2016). Fluid elements along a materially invariant boundary have the same average angular speed and vorticity, and thus equally large LAVD values. Accordingly, an RCLV is identified

in the LAVD field as a closed contour surrounding a local maximum (Haller et al., 2016; Tarshish et al., 2018). The RCLV represents a feature that maintains coherency from $\tau = t_0$ to $\tau = t_1$.

170   We calculated the 32-day, backward-in-time LAVD for every Lagrangian particle in 920 simulations. The LAVD field is visualized by plotting the value for each particle at the initialization time and location (see Fig. 1(a)). Moving forward, we refer to the initialization dates of each of the LAVD fields as the "timesteps" of our dataset (each separated by eight days), since this is the frequency at which RCLVs boundaries were identified. The Python package *floater* was used to identify RCLVs from local LAVD maxima encompassed by closed contours (Tarshish et al., 2018). The algorithm has several free parameters

175   that must be carefully chosen, as they affect what qualifies as an RCLV boundary. This includes minimum area, minimum distance between features, and the contour Convex Deficiency (CD).

     Since the LAVD field has a finer spatial resolution than the SLA field, we can detect smaller RCLVs than SLA eddies. Moreover, RCLV radii tend to be half the length of SLA eddy radii (Abernathey and Haller, 2018; Liu and Abernathey, 2023). Assuming a 20 km minimum radius, a circular feature of this size would have an area of 1257 km^2 or contain roughly 104

180   grid cells ($1/32°$). Therefore, we set the minimum RCLV area to 104 grid cells. The minimum RCLV radius of 20 km is roughly equivalent to the length scale of six or more grid cells, so for the edge of two minimally sized RCLVs to be touching the distance between their centers will be 12 grid cells. Assuming that RCLV eddy centers are at least an "eddy distance" away from each other, we set the minimum distance between the local maxima of the LAVD field to 24 grid cells.

     The CD is the ratio of a contour area to its convex hull (Haller et al., 2016), where the convex hull is the closed curve with

185   the shortest perimeter containing the polygon. In the context of the LAVD field, an RCLV contour with a low CD presumably contains a fluid structure with minimal filamentation. Choosing a threshold for the CD is somewhat arbitrary since the boundaries of two different vortices with the same CD can have differing degrees of dispersal. Tarshish et al. (2018) introduced a complementary metric to the CD called the Coherency Index (CI). The CI measures the spatial compactness of a set of Lagrangian particles over time, defined

190   $$CI = \frac{\sigma^2(0) - \sigma^2(t)}{\sigma^2(0)} \qquad (4)$$

where $\sigma^2(t) = <|\boldsymbol{X}(t) - <\boldsymbol{X}(t)>|^2>$ is the variance of the particle positions at time t, and the $<>$ symbols indicate the mean. $<\boldsymbol{X}(t)>$ is the mean position of all particles or the feature center. A low CI indicates that the particle set has spread apart over the time frame, whereas a high CI indicates compressing behavior.

     Tarshish et al. (2018) correlated CI with various choices of CD in order to select a threshold CD to define a coherent eddy.

195   Informed by our sensitivity tests, we refined their method by searching for the largest contour surrounding a local maximum that satisfies the conditions $CD <= 0.03$ and $CI >= -0.5$. Because CD and CI are not linearly correlated (Fig. B1), we found that this is an appropriate, conservative measure to identify robust structures with limited filamentation. Figure 2 shows particle trajectories initialized inside four different potential contour boundaries of an RCLV. Only the smallest contour with target $CD = 0.01$ passed the criterion of $CD <= 0.03$ and $CI >= -0.5$.

200   In some rare cases, RCLV contours passed the CD and CI thresholds but did not encompass a single materially invariant vortex. The LAVD metric is derived from the absolute value of the relative vorticity, thus filamentations of opposite polarity
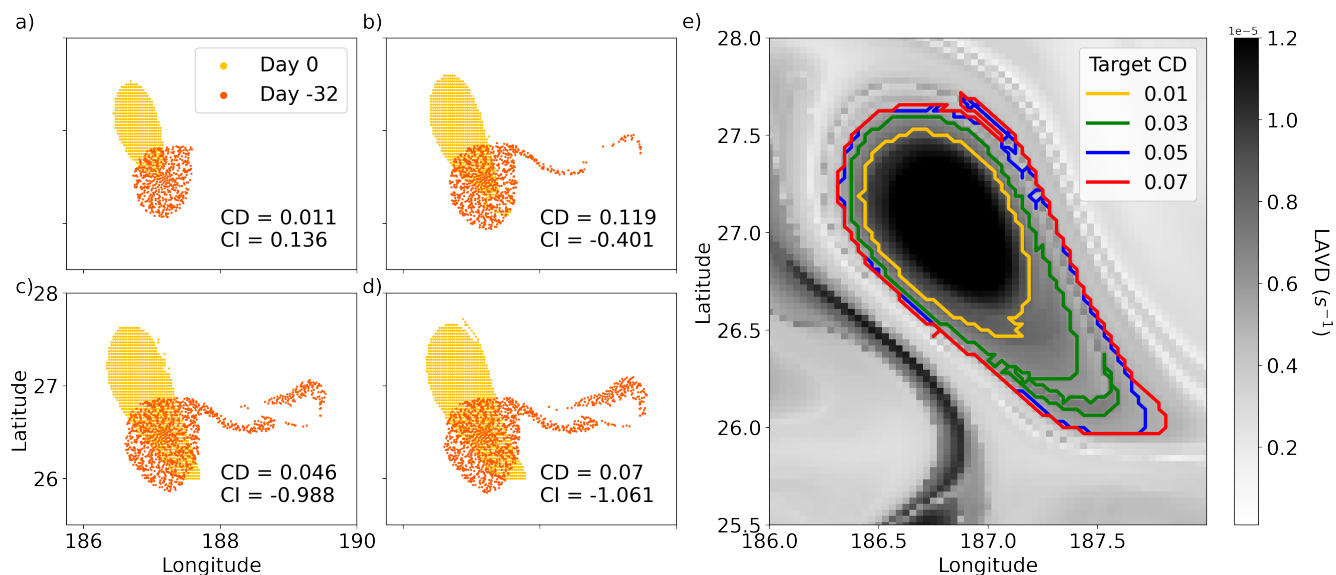
Figure 2. An RCLV vortex and its potential boundaries. (a) Particles were initialized inside the target $CD = 0.01$ contour and advected backward in time for 32 days. The particles are yellow at the initialization, and orange at their locations after advection. (b) Target $CD = 0.03$. (c) Target $CD = 0.05$. (d) Target $CD = 0.07$. (e) Contour output from different target CDs.

could occur amongst particles in a supposed RCLV contour so long as they maintain integrated vorticity of a high magnitude. In order to exclude such behavior from our dataset, we ran sensitivity tests that determined the requirement for 85% of particles within a contour to have the same sign of the vorticity at the beginning and end of the simulations. Thus to qualify as an RCLV,

205 if at least 85% of particles in a feature had negative (positive) vorticity at the initialization of the simulation, 85% must also have had negative (positive) vorticity 32 days previously. This requirement is a more conservative identification of RCLVs than in previous literature, but one that we found necessary to identify robustly coherent features. We assigned RCLV polarity by the dominant sign of the vorticity of the particles inside of the boundaries, where cyclones (anticyclones) had a positive (negative) sign of relative vorticity.

210 The RCLV parameters were selected to delineate boundaries that contain minimally filamentous vortices, as exhibited in Fig. 2. Depending on the scientific application, one might choose alternative criteria for eddy coherency or choose different parameter values when analyzing a different dataset. The parameter choices made for this study are summarized in Table 1.

2.4.2 RCLV tracking

On account of our strict thresholds for RCLV boundaries, following the advection pathway of a single particle was sufficient

215 to track coherent water masses between the 8-day timesteps. To do so, we used the same Lagrangian trajectories that were simulated to compute the LAVD. For each unique coherent water mass, the algorithm proceeds as follows:

1. Starting at the last chronological timestep (on July 4th in Fig. 3), the RCLV is assigned a unique ID.

Table 1. Summary of free parameters

SLA eddies	
Minimum age	32 days
Minimum area	12 grid cells $(1/4°)$
Disappearance tolerance	3 days
Lagrangian simulations	
Initial particle resolution	$1/32°$
Particle timestep	20 minutes
Output frequency	6 hours
Run time	32 days
Re-initialization frequency	8 days
RCLVs	
Minimum area	104 grid cells $(1/32°)$
Minimum distance between centers	24 grid cells
Maximum CD	0.03
Minimum CI	-0.5
Minimum vorticity consistency	85%
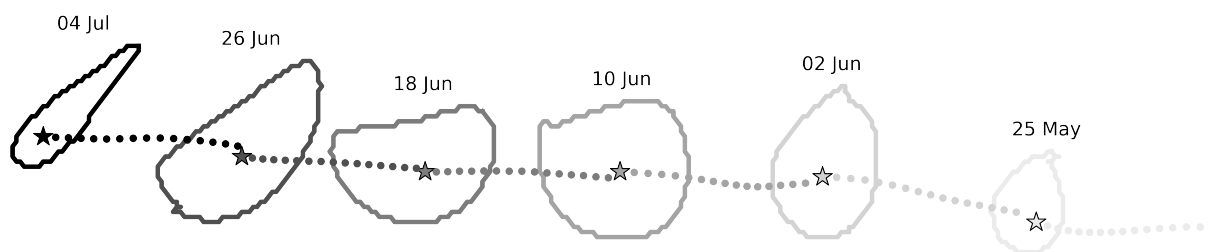
Figure 3. Illustration of the vortex tracking method for an RCLV transiting westward. The solid lines represent the RCLV contours every eight days, the stars indicate the location of the local maxima of the LAVD at the corresponding timestep, and the dots represent the backward trajectory of the Lagrangian particle to the previous timestep. The water mass developed into a coherent structure 32 days prior to May 25th and remained coherent until July 4th. The contours and particle trajectories were artificially spread apart here for visual purposes.

2. The Lagrangian particle corresponding with the LAVD local maximum is tracked backward in time (from July 4th to June 26th in Fig. 3). This represents the center of the rotating rigid body and is the particle most likely to remain inside of the vortex for the extent of its lifetime.

3. If the Lagrangian particle is advected into a contour in the previous chronological timestep (June 26th in Fig. 3), then that RCLV contour is also assigned the unifying ID.

4. Repeat Steps 2. and 3. until the particle is not advected inside a contour in the previous chronological timestep (on May 25th in Fig. 3). This represents the RCLV birth, i.e. the first timestep that the eddy was coherent for at least 32 days.

5. The RCLV instances are assigned an age, with the first chronological contour called 32 days old (on May 25th in Fig. 3).

Although the feature in Fig. 3 contains the same core water mass from May 25th to July 4th, the vortex changes in size with time. Our method inherently allows the RCLV to have a fluctuating material belt on the eddy periphery Xia et al. (2022a) because the contours are detected independently at each timestep. In other words, each contour contains fluid that was part of the RCLV for at least 32 days, but all of the fluid need not be part of the structure for the full lifespan of the tracked eddy. Each instantaneous contour represents the coherent boundary at that time, but in most cases, only an inner core is part of the coherent structure for the entirety of the RCLV lifetime. This method captures the RCLV evolution that a phytoplankton population would realistically be subject to.

2.4.3 Disappearing RCLVs

We found some cases where two RCLV contour sets encompass the same fluid mass, but the eddy "disappears" for one or more timesteps. This could occur if a coherent structure reduced in size below the minimum threshold, or the RCLV contour at the skipped timestep had a CD or CI just outside of the parameter limits. Other possibilities include an eddy splitting or merging event. To avoid prematurely terminating an eddy, our algorithm allows RCLVs to disappear for up to two timesteps for the purposes of accurately attributing RCLV age and examining feature evolution. In order to interpolate through this disappearance, the Lagrangian trajectories of particles inside of the first chronological contour following the skipped timestep(s) are tracked backward in time. A polygon is drawn around the mass of particles at each missing timestep, and all contours are linked with a unifying RCLV ID number. 9.4% of contours in our published dataset were interpolated in this manner and are flagged.

3 Results

In this section, we present a summary and key features of the 20-year comparison of RCLVs and SLA eddies in the NPSG. Figure 1 portrays a comparable density of RCLVs and SLA eddies in the region and shows that numerous features were identified with both methods, though many were only identified in one. Video S1 displays the dynamic evolution of the LAVD, SLA, and eddy boundaries over one year. The Video illustrates that most eddies transit westward in the domain such that their displacement is influenced by the large-scale flow.

Table 2. Number of eddies from 2000-2019

	All	**Anticyclonic**	**Cyclonic**
RCLV instances	40644	18200	22444
Tracked RCLV IDs	11900	5615	6285
Daily average number of RCLVs	44.2	19.8	24.4
SLA eddy instances	28482	13395	15087
Tracked SLA eddy IDs	5990	2858	3132
Daily average number of SLA eddies	31.0	14.6	16.4

Only includes eddies that are 32 days old or more with an 8-day detection frequency.

The number of eddies in the RCLV and SLA atlases are summarized in Table 2. The RCLV atlas contains 40,644 contours, with 11,900 unique IDs associated with features tracked within the bounds of the domain. Daily-resolved atlases would have 8 times as many contours as presented here, but the same number of IDs/tracked features. On any given day, there are on average 44 RCLVs. SLA eddies are less frequent, with 5,990 unique IDs and a mean of 31 per day. The lower frequency of SLA eddies compared to RCLVs is in part due to the stricter size thresholds. However, we cannot accurately detect smaller Eulerian eddies with the current spatial resolution of remotely sensed SLA ($1/4°$). Cyclonic eddies are more frequent than anticyclonic eddies in both datasets, although this bias varies regionally (see Section 3.3).

The median lifespan for tracked RCLVs is 40 days, compared to 55 days for SLA eddies. SLA eddies tend to have a longer lifespan than RCLVs except for in the Lee of Hawai'i. Even so, the Lee Eddies are the longest-lived features in both datasets. Eddies in the southeast quadrant can also have long lifespans (upwards of 100 days) as they transit westward toward the south of the islands. In the remainder of the domain, RCLVs do not typically survive beyond 64 days. We did not find significant differences in eddy age between the polarities in either dataset.

We compared the co-occurrence of eddy contours in the SLA and RCLV atlases at each 8-day timestep, the results of which are presented in Fig. 4. SLA eddy contours that do not co-occur with an RCLV are referred to as "non-overlapping" SLA eddies as opposed to co-occurring "overlapping" eddies (Liu et al., 2019). We found that 57% of cyclonic and 51% of anticyclonic SLA eddy contours overlap with an RCLV. Over the lifetimes of tracked SLA eddies, 67% of cyclones and 62% of anticyclones overlap with RCLVs at some point. This suggests that while roughly two-thirds of SLA eddies trap material during their lifetime, only half have significant retentive properties at any given time. More RCLVs were identified than SLA eddies, thus 63% of cyclonic and 65% of anticyclonic RCLVs never overlap with SLA eddies.

3.1 Temporal variability

RCLVs and SLA eddies have similar annual and interannual variability, as shown in Fig. 5, suggesting common underlying mechanisms. The monthly average eddy frequency data that underlies Fig. 5(b) is provided in Appendix Table C1. Daily eddy frequency peaks in June and July and is lowest in December and January, consistent with previously noted summer peaks of
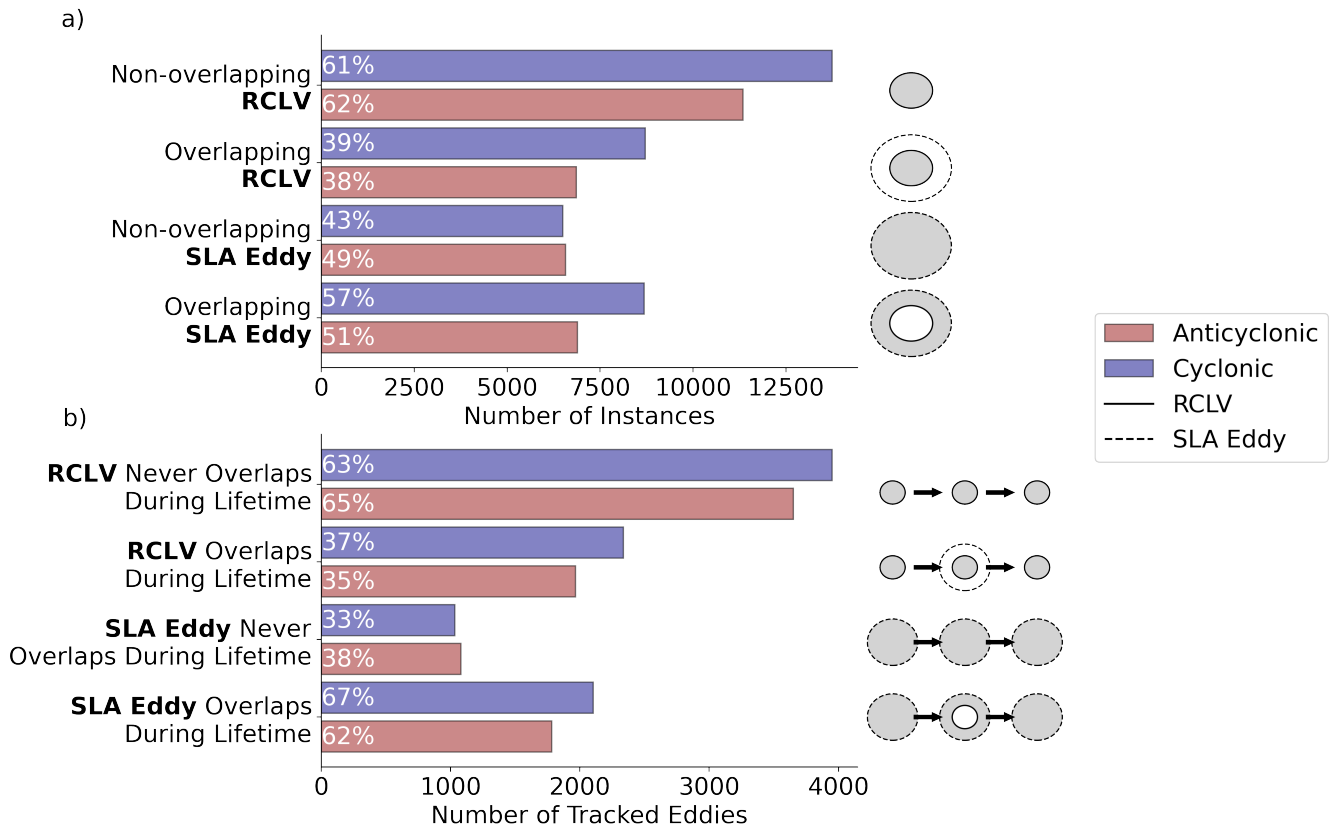
Figure 4. (a) The number of eddy contours that are concurrent ("overlapping") and not concurrent ("non-overlapping") with contours in the other atlas. The percentages of eddies exhibiting the given characteristic compared to the total number of eddies of each polarity are overlaid in white. For overlapping eddies, the numbers are the same since this is a mutual metric, but the percentages of the total eddy counts differ. The schematics on the right-hand side show the referenced feature in gray. (b) The number of eddies that overlap and never overlap throughout the lifetimes of the tracked features.

eddy kinetic energy (EKE) in subtropical gyres (Zhai et al., 2008). Nevertheless, by only including eddy occurrences that are 32 days of age or older, the seasonal peak presented here may be shifted later in the year than if we were to include the younger eddy phases. We found that, on any given day, there tend to be 25% more anticyclonic and 32% more cyclonic RCLVs than
275 SLA eddies.

Possible explanations for the annual cycle of mesoscale activity include seasonal changes in thermal interactions with the atmosphere (Rieck et al., 2015), seasonality in the conversion of eddy potential energy into kinetic energy (Guo et al., 2022), and the inverse energy cascade of increased submesoscale activity in the winter to mesoscale activity in the summer (Sasaki et al., 2017; Uchida et al., 2017; Schubert et al., 2020). We found no significant trend in changes in eddy frequency from 2000-
280 2019, and deviations from the annual mean often co-occur in the RCLV and SLA eddy datasets (Appendix Fig. C1). Interannual
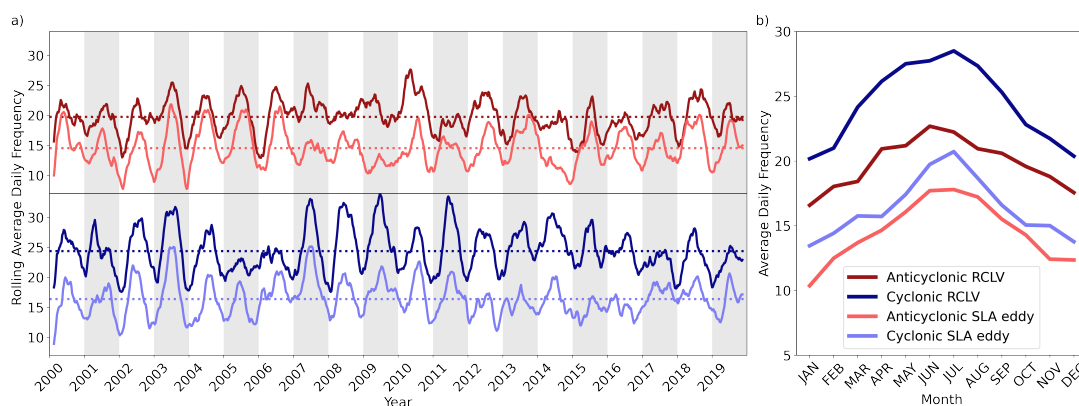
Figure 5. (a) RCLV and SLA eddy rolling mean frequency from 2000-2019. Frequency refers to the number of eddies per 8-day timestep. The horizontal dotted lines show the mean frequency for each feature type. (b) Monthly average RCLV and SLA eddy frequency.

changes are likely driven by large-scale climate variability. For example, submesoscale activity is more active in El Niño winters in this domain, and by the inverse energy cascade, this modulates mesoscale interannual variability (Sasaki et al., 2022). During positive phases of the Pacific Decadal Oscillation, the vertical shear between the Hawaiian Lee Countercurrent and the North Equatorial Current increases, enhancing baroclinic instability and EKE in the Hawaiian Lee Eddy region (Yoshida et al., 2011). Similarly, positive phases of the Pacific Decadal Oscillation drive baroclinic instabilities and increased EKE to the northeast of the Hawaiian Islands (Chen and Qiu, 2010).

3.2 Eddy size

We found large variability in the eddy area as RCLVs evolve through time. For RCLVs that lived longer than the minimum 32 days (N = 7059), the median relative change in areas between the 8-day timesteps is 21% and the mean is 51% (Appendix Fig. D1). This supports the need for a high temporal resolution to capture details of the boundary evolution of material coherence. A dominant pattern emerges in the changes in area throughout RCLV lifetimes. We found that following the initial 32-day detection, RCLVs tend to grow for the next 20% of their lifespan, then maintain their area, and finally decrease in size during the last half of their life (Appendix Fig. D2).

SLA eddies tend to be substantially larger than RCLVs, consistent with previous studies (Abernathey and Haller, 2018; Liu et al., 2019; Xia et al., 2022b; Liu and Abernathey, 2023). The RCLV median area is $5,203\ km^2$ and $25,369\ km^2$ for SLA eddies. For the cases of overlapping eddy boundaries, SLA eddies are on average 4.7 times the size of RCLVs (Appendix Fig. D3). A comparison between eddy maximum area and lifespan is shown in Fig. 6, revealing a positive linear relationship ($R^2 = 0.668$) for RCLVs. In other words, the larger an RCLV, the longer it tends to remain coherent. SLA eddies show a weaker relationship between maximum area and lifespan ($R^2 = 0.404$). There are many cases of large SLA eddies with a relatively short lifespan and small SLA eddies with long lifespans. This suggests that RCLV boundaries have a more mechanistic
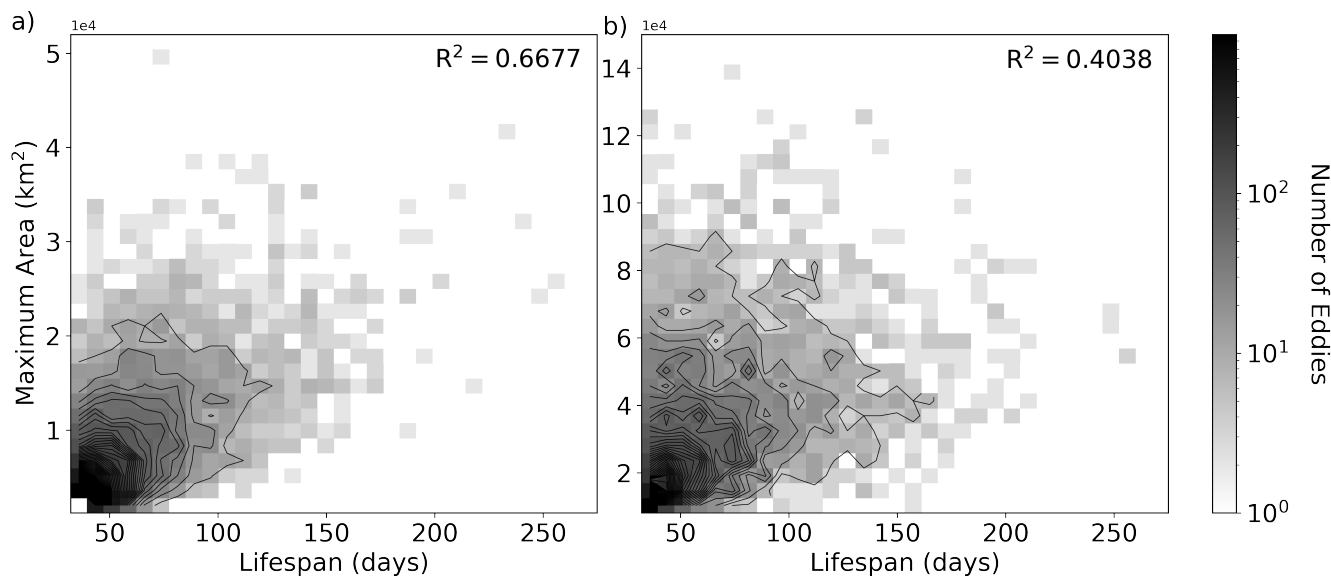
Figure 6. 2D histogram of maximum area versus lifespan for (a) RCLV and (b) SLA eddies from 2000-2019. The contours of the histogram distributions are overlaid in black.

relationship with eddy longevity than SLA eddy boundaries. Overall, these results emphasize that a critical difference between RCLV and SLA eddies is the feature size.

3.3 Spatial variability

We assessed the spatial variability of the mesoscale activity from the RCLV and SLA eddy atlases across the NPSG. In Fig. 7,
305 eddy frequency was calculated from the number of times each coordinate point was contained within an eddy boundary. The highest frequencies of both RCLVs and SLA eddies are in the Lee of the Hawaiian Islands. The Lee Eddies have two distinct pathways during their westward transit: 1) hugging the islands traveling northwest and 2) southwest. This results in a sideways V-shaped pattern in the spatial eddy frequency to the west of the Hawaiian Islands. Excluding the Lee of Hawaiʻi, eddies are generally evenly distributed across the domain, with marginally more activity to the east of the islands than to the west. The
310 lower frequencies on the domain edges are an artifact of the requirement for the full eddy boundaries to be located inside of the domain. We found that the likelihood of being inside an SLA eddy is higher than being in an RCLV since SLA eddies tend to be larger.

The polarity probability (P) is defined

$$P = \frac{(F_A - F_C)}{(F_A + F_C)} \tag{5}$$

315 where F_A is the frequency of anticyclones, and F_C is the frequency of cyclones Chaigneau et al. (2009). When $P > 0$ ($P < 0$), anticyclonic (cyclonic) eddy polarity is more common at the given location. Figure 8 shows the geographic distribution of
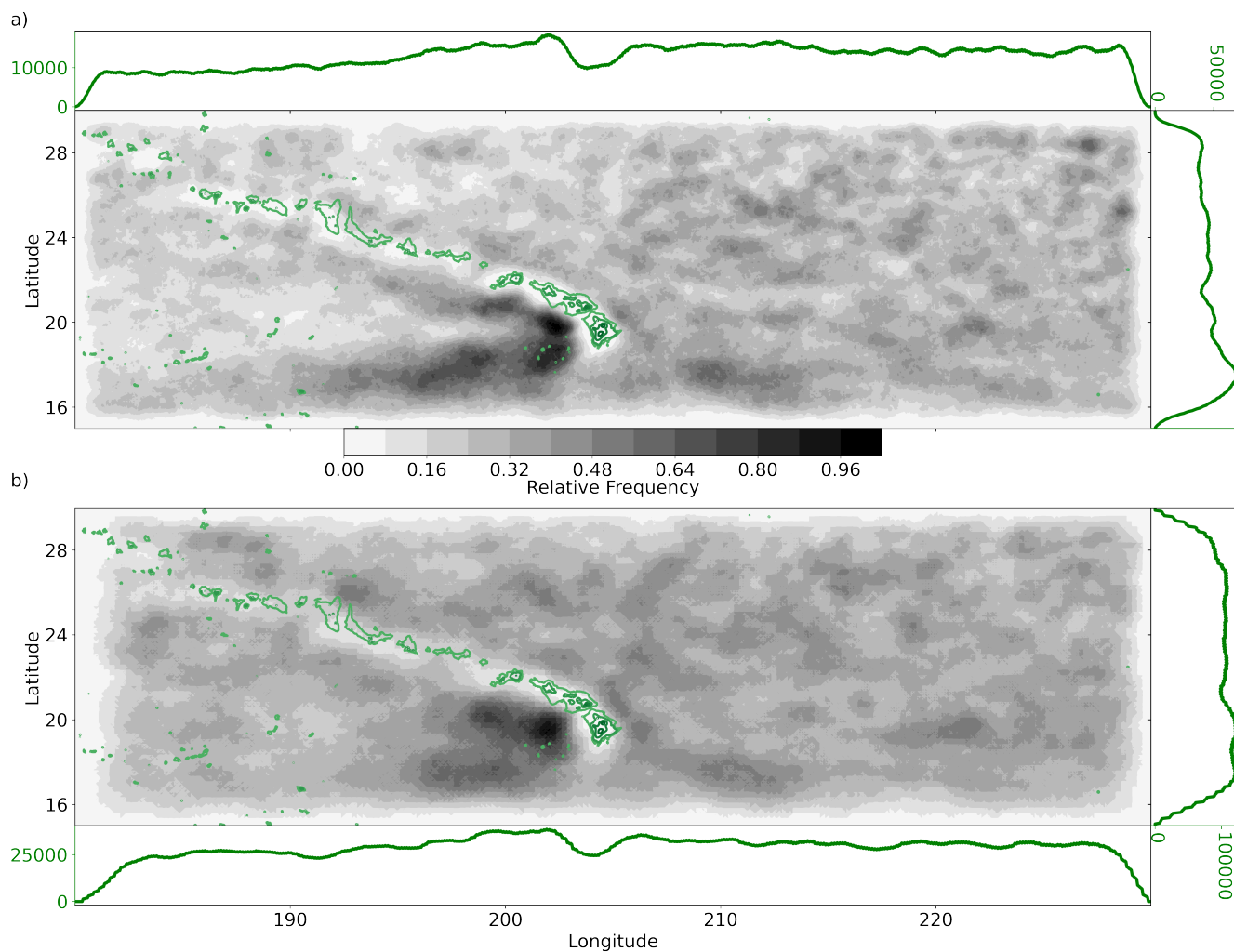
Figure 7. Geographic distribution from 2000-2019 of (a) RCLVs and (b) SLA eddies. The green line plots along the horizontal (vertical) represent the number of times an eddy was present at that longitude (latitude). Frequencies include all coordinate points contained within eddy boundaries. The overlaid green contours show the bathymetry (GEBCO, 2023) above 2000 m below sea level, including the Hawaiian Islands and underwater seamounts.

polarity probability of (a) RCLVs and (b) SLA eddies. The differences are particularly striking in the region of the Hawaiian Lee Eddies to the west of the islands, where SLA eddies have a much weaker polarity probability. This is driven by a disparity in anticyclonic eddy detection between the RCLV and SLA eddy datasets (Appendix Fig. E1). A large quantity of SLA eddies hugging the west of the islands is detected with no corresponding equivalent in the RCLV atlas. This suggests that a subset of anticyclonic Lee Eddies are not coherent.

320
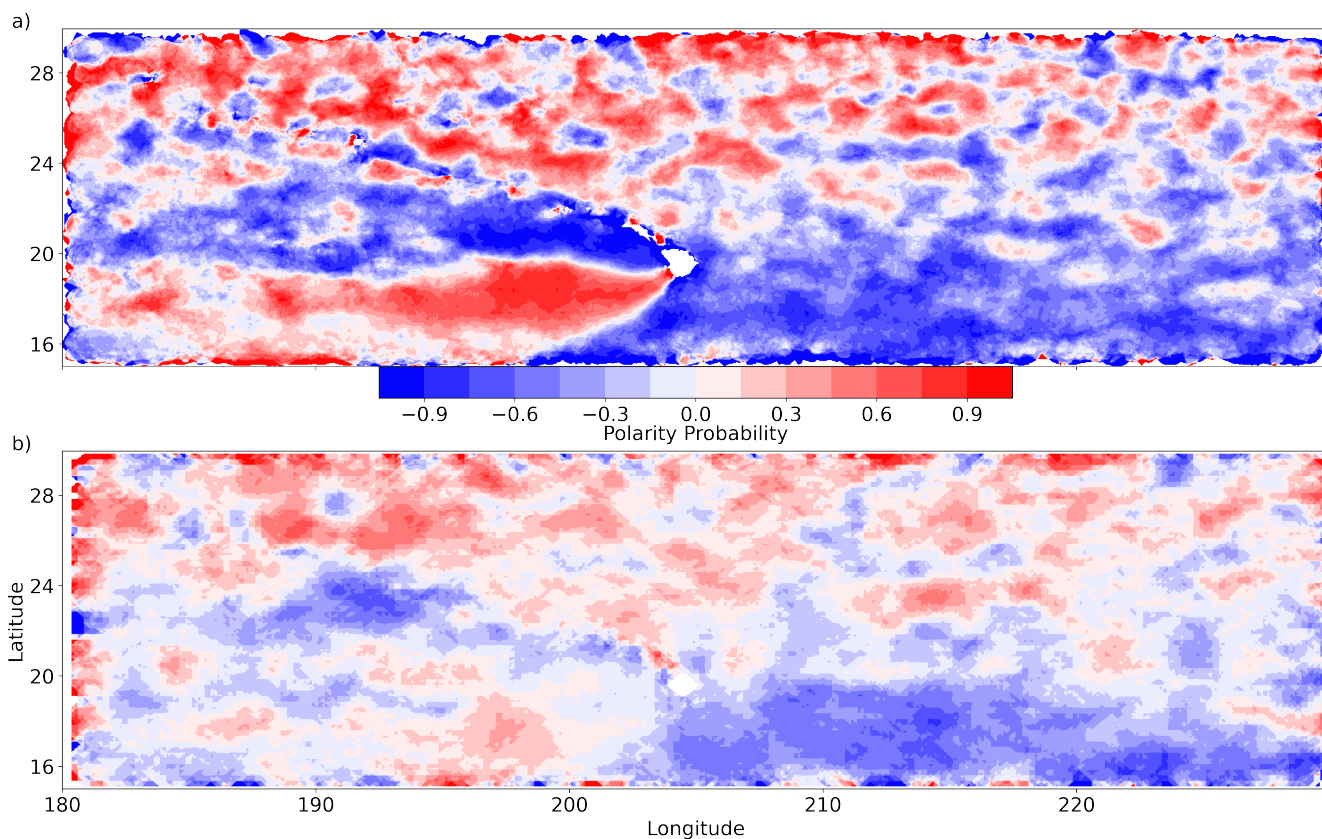
Figure 8. Polarity probability from 2000-2019 for (a) RCLVs and (b) SLA eddies. $P < 0$ (blue) indicates more cyclonic activity, and $P > 0$ (red) more anticyclonic activity.

There is more anticyclonic activity in the northern half of the domain from 23-30°N in both datasets, whereas cyclones are much more frequent in the southeast quadrant from 15-23°N. This is consistent with previously published studies that find latitudinal bands of eddy polarity probability across the global ocean, including similar structures in our domain (Chelton et al., 2011b; Dong et al., 2022). The process by which these bands are generated remains unclear. Nevertheless, we find distinct regional mesoscale provinces generated by the polarity of eddies, which is of particular interest for biogeochemical applications since phytoplankton respond differently to cyclones and anticyclones. The RCLV dataset reveals a more striking banded pattern by latitude, whereas in the SLA dataset, the transitions are fuzzier. This divergence is driven by the larger areas of SLA eddies, which act to extend the ranges of eddies of each polarity. To bolster this point, Appendix Fig. E3 reveals the distributions of polarity exclusively from eddy centers. The differences between the atlases, in this case, are minimal except for in the Lee of Hawaiʻi (Appendix Fig. E4).

3.4 Chlorophyll-*a* in a coherent eddy: A case study

Hawaiian Lee cyclones have been influential in the study and thinking of the mesoscale structuring of chl-*a* and ocean productivity. The cyclonic vorticity is associated with an adiabatic uplift of nutrient-rich isopycnals into the euphotic zone, stimulating
335   primary production and blooms of phytoplankton, a process termed "eddy-pumping" (Falkowski et al., 1991). The resulting chl-*a* blooms in Lee cyclones are clearly documented in both in situ data and remote sensing (e.g., Falkowski et al., 1991; Seki et al., 2001; Vaillancourt et al., 2003; Benitez-Nelson et al., 2007; Benitez-Nelson and McGillicuddy Jr, 2008; Calil and Richards, 2010). The intensity of a mesoscale chl-*a* feature should depend, in part, upon the rate of dilution with surrounding waters.

340   To illustrate the utility of the RCLV atlas, we examined how Lagrangian coherency influences the interpretation of chl-*a* in a long-lived Hawaiian Lee cyclone (RCLV ID 6724). Panels (a) and (b) of Fig. 9 show the 8-day average chl-*a* concentration from 9-17 May 2010. On May 17th, the SLA eddy contour is 78 days old and the RCLV eddy contour is 56 days old. This discrepancy in age occurs because the eddy was not coherent during early formation, and thus it appears as a dispersive SLA eddy before developing an RCLV in its core. Toward the end of the eddy life, the RCLV persists for over a month longer than
345   the SLA eddy. An SLA eddy may disappear prematurely, such as in this case, if the SLA anomaly flattens below the detection limit or if the boundary area reduces below the size thresholds. Video S2 shows the eddy contours and chl-*a* evolution from genesis to dissolution.

We expect the coherent core, identified by the RCLV boundaries, to be less affected by lateral dilution with surrounding waters than the outer ring of the SLA feature. This is illustrated in Fig. 9(c), which shows the eddy boundaries on May 17th (in
350   black) and April 23rd (in gray). The blue line is the trajectory of a Lagrangian particle between those dates. It remains inside of the eddy because it is nested in the interior of the RCLV. The orange line shows the trajectory of another Lagrangian particle that is inside of the SLA bounds, but outside of the RCLV. The orange particle was not inside of the eddy on April 23rd but rather originated from waters near the Hawaiian Islands. This demonstrates the difference in fluid retention between the eddy types.

355   The chl-*a* anomalies inside of the respective eddy contours over the feature lifetime are shown in Fig. 9(d). The chl-*a* anomaly is defined as the difference between the mean chl-*a* in the region of twice the radius of the eddy boundary and the mean chl-*a* inside of the boundary. The chl-*a* anomaly in the SLA eddy exceeds the RCLV anomaly only at one timestep (July 12th), despite the fact that the RCLV is usually nested inside of the SLA bounds. To further highlight the contribution of the RCLV to elevated chl-*a* inside of the eddy, we plotted (in red) the anomaly inside of the SLA eddy contour, excluding the
360   RCLV. In this dispersive zone of the eddy, the chl-*a* anomaly is lower than the all-encompassing SLA eddy at every timestep. A viable interpretation is that the RCLV is trapping and transporting a phytoplankton community, whereas the biomass in the non-retentive zones of the SLA eddy is quickly diluted by mixing with surrounding waters. This example illustrates that the measured chl-*a* anomaly associated with an eddy can be vastly different depending on how one defines the eddy boundary.

Likely due to a shoaling mixed layer, chl-*a* increases in both the SLA and RCLV in May, the month that the mixed layer
365   depth is the shallowest in the region (Rii et al., 2022). Chl-*a* then subsequently declines for several weeks until August when
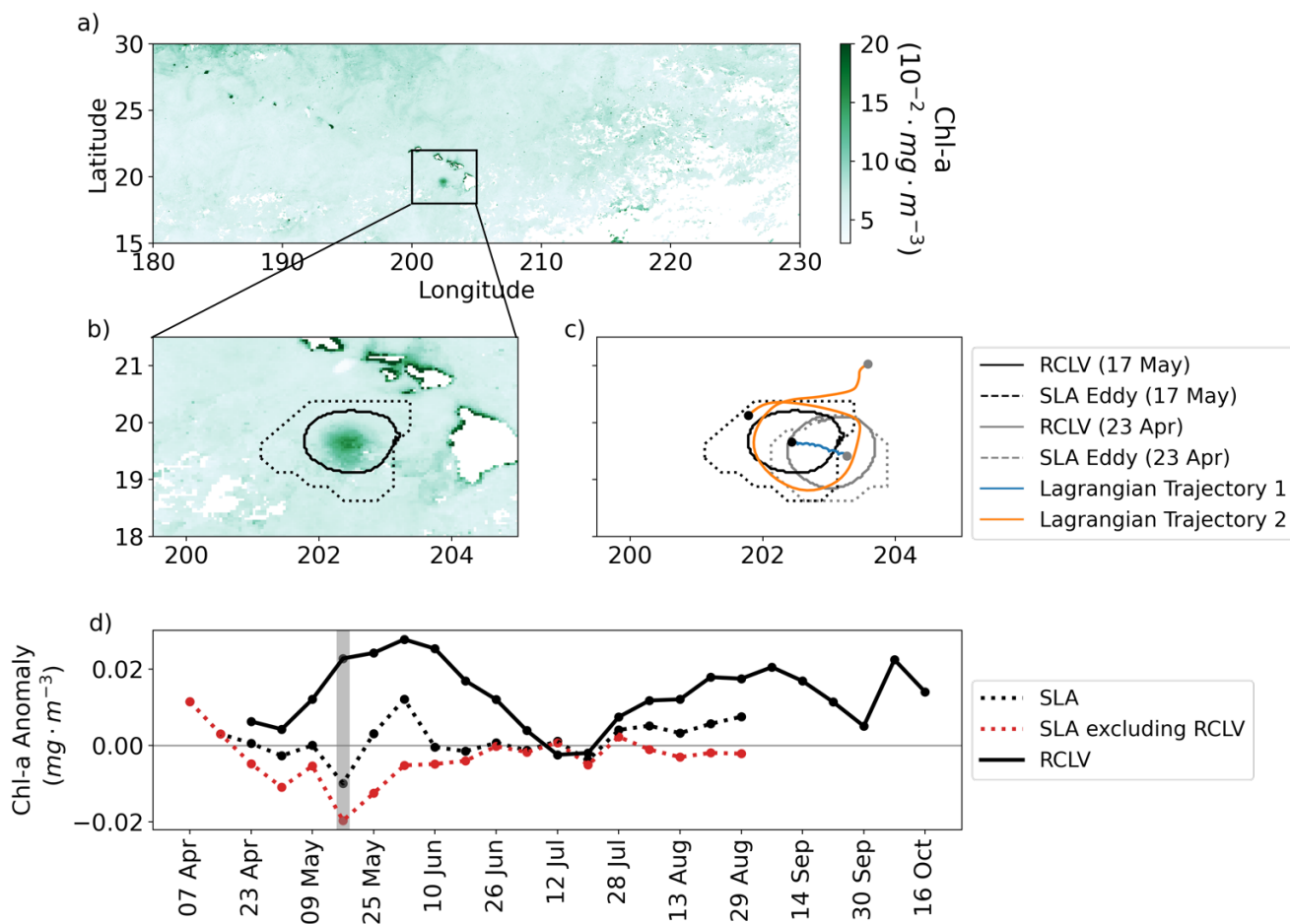
Figure 9. Chl-*a* in a Hawaiian Lee cyclone. (a) 8-day average chl-*a* from 9-17 May 2010. (b) Same as (a), but zoomed in on the anomalous chl-*a* patch. The solid line represents the RCLV contour on May 17th and the dashed line represents the SLA eddy contour. (c) A comparison of eddy boundaries on May 17th and 24 days prior on April 23rd. The Lagrangian trajectory of a particle from the interior of the RCLV is plotted in blue (Lagrangian Trajectory 1). The trajectory of a particle inside of the SLA eddy boundary but outside of the RCLV on May 17th is plotted in orange (Lagrangian Trajectory 2). Over 24 days, this particle entered the eddy bounds from surrounding waters to the north. (d) Average chl-*a* anomaly inside of the boundaries over the eddy lifetime. The red dashed line displays the average chl-*a* inside of the SLA eddy boundary, but outside of the RCLV. The dots depict the 8-day frequency of the eddy atlases and the gray bar highlights the chl-*a* concentration corresponding with panels (a) and (b) on May 17th.

there is a second increase. We hypothesize that the August bloom is caused by non-mesoscale processes, but that the chl-*a* signature is emphasized in the RCLV due to trapping. The end of August marks the demise of the SLA feature, but Video S2 shows that the chl-*a* concentration continues to be higher inside of the RCLV than in surrounding waters. This highlights that coherent mesoscale circulations may continue to modulate chl-*a* beyond the detection limit of the SLA method.

4 Discussion

We presented an atlas of Lagrangian coherent mesoscale eddy boundaries in the North Pacific Subtropical Gyre (NPSG), spanning two decades and designed with several unique features focused toward biogeochemical applications. Key aspects of the methodology are the 8-day frequency synchronized to ocean color products, backward-in-time Lagrangian analysis, and eddy tracking. By comparing Lagrangian (RCLVs) and Eulerian (SLA) mesoscale eddy boundaries, we showed that there are clear distinctions in size and lifespan. On the other hand, the temporal and spatial variabilities are similar for RCLVs and SLA eddies, suggesting that both datasets capture mesoscale activity that is modulated by analogous mechanisms.

We tracked 11,900 unique RCLVs and roughly half as many SLA eddies. Only half of the eddies detected from the SLA contain a Lagrangian coherent structure (as defined in this study). However, two-thirds of SLA eddies overlap with RCLV at some point in their lifetime. In other words, a third of mesoscale eddies detected from the SLA are never coherent and experience a significant exchange of material with surrounding waters over their whole lifetime. Only 36% of the tracked RCLVs are concurrent with an SLA eddy boundary at some point in their lifetime, indicating that a majority of coherent eddies may be missed by SLA identification entirely.

RCLVs that do not overlap with an SLA eddy for their entire lifetime have significantly shorter lifespans (median 32 days) than their overlapping counterparts (median 72 days). Of the tracked RCLVs that do overlap with an SLA during their lifetime, 54% develop prior to the detection of the SLA eddy boundary and 66% continue to propagate after the concurrent SLA eddy is no longer detectable. This suggests that the majority of the occurrences of non-overlapping RCLVs are short-lived features, developing SLA eddies, or the remnants of SLA eddies. We hypothesize that elevated chl-a at the onset of SLA eddy detection may be enhanced due to early trapping of an initial anomaly.

Using the definitions applied here, RCLVs tend to be much smaller than SLA eddies. We found that the areas of the RCLV boundaries have a linear relationship with lifespan (Fig. 6). The comparatively large SLA boundaries have a weaker relationship with eddy lifespan and act to dilute the underlying spatial distribution of eddy polarity as manifested in the RCLV dataset (Fig. 8). Although RCLV and SLA eddy boundaries encompass mechanistically similar or equivalent mesoscale features, it is important to consider the lenient boundaries derived from SLA detection methods when interpreting biogeochemical observations categorized as "inside" or "outside" of an eddy.

We detected many coherent vortices that have an elongated shape. Obvious examples of this include the overlapping anticyclonic RCLV and SLA eddy north of the islands and below the legend at coordinates $(202.3°, 22.8°N)$ in Fig. 1, and the RCLV on July 4th in Fig. 3. Commonly used eddy detection algorithms (e.g., AVISO products Chelton et al., 2011b; Mason et al., 2014) penalize features that are less circular and potentially miss coherent mesoscale eddies. An advantage of the OceanEddies algorithm used here is that it is parameter-free with respect to eddy shape (Faghmous et al., 2015). Nevertheless, it would be informative to directly compare the RCLV atlas with other eddy datasets such as the AVISO Mesoscale Eddy Trajectory Atlas Product (Mason et al., 2014; Pegliasco et al., 2022) or the OW method. We included a comparison of the RCLV and SLA eddy datasets to the OW parameter from a single day in Appendix Fig. A1.

4.1 Hawaiian Lee Eddies and implications for chlorophyll-*a*

The Hawaiian Lee Eddies generate the strongest signals of eddy activity in this domain, falling into two distinct groups. The
405 first are long-lived anticyclonic eddies generated by the instability of the shear between the eastward flowing Hawaiian Lee
Countercurrent and the westward flowing North Equatorial Current (Calil et al., 2008; Yoshida et al., 2010; Liu et al., 2012).
These anticyclones travel westward in the latitude band between 15-20°N. The second group includes cyclones induced by a
wind stress curl anomaly associated with the blocking of the trade wind (Lumpkin, 1998; Yoshida et al., 2010). These cyclones
hug the western side of the Hawaiian Islands while transiting toward the Hawaiian Lee Current between 20-24°N (Lumpkin,
410 1998). We found that both groups of Lee Eddies have predictable translation pathways, are strongly coherent, and are long-
lived. However, a subset of anticyclonic Lee Eddies that hug the islands only appear in the SLA eddy dataset. This suggests
that some of the Lee Eddies are not coherent on the timescales explored in this study.

The consistent generation and pathways of Hawaiian Lee cyclones have made them a key tool in the study of the biogeo-
chemistry of ocean eddies (e.g., Falkowski et al., 1991; Seki et al., 2001; Vaillancourt et al., 2003; Benitez-Nelson et al., 2007;
415 Benitez-Nelson and McGillicuddy Jr, 2008; Calil and Richards, 2010). However, due to their strong trapping capacity and con-
sistent paths of propagation, they may not be representative of the shorter-lived and less coherent eddies generated elsewhere
in the domain (e.g., at Station ALOHA located north of the Hawaiian Islands (Barone et al., 2019; Rii et al., 2022)). We hy-
pothesize that the biological signature of eddies will vary depending on their trapping behaviors and the manner by which eddy
boundaries are defined, as exhibited in Fig. 9. We have a follow-up manuscript in preparation using the RCLV atlas presented
420 here to examine the influence of eddy trapping on surface chl-*a* across the domain.

4.2 Even RCLVs are "leaky"

A consideration when employing any such analysis with the geostrophic approximation is that the identified coherent features
are not truly closed systems at the ocean surface. The ageostrophic component of the flow is not resolved in the SLA-derived
flow fields used to evaluate particle trajectories in this study. In fact, the LAVD method fails to identify RCLVs at the surface
425 in high-resolution simulated velocity fields that include ageostrophic motions (Sinha et al., 2019; Xia et al., 2022b; Ntaganou
et al., 2023). There can be mixing at the margins of eddies due to submesoscale instabilities, and the two-dimensional nature of
this analysis misses the effects of vertical motions and mixed layer thickening. Despite these considerations, we still observed
concentrated patches of chl-*a* within coherent eddy boundaries, such as in Fig. 9. This suggests that, in this case, the timescale
of unresolved fluxes through the coherent boundaries is slower than the biological processes, and thus the localized bloom is
430 contained or enhanced. Mesoscale geostrophic structures penetrate below the mixed layer in this region (Liu et al., 2012, 2020),
so RCLVs identified from the surface geostrophic flow may also reflect lateral trapping deep in the water column where chl-*a*
tends to be at a maximum. In a 3D simulation of the Gulf of Mexico and the Caribbean Sea, Ntaganou et al. (2023) identify
RCLVs as deep as $800\ m$. There is a need for more estimates of RCLV penetration depth and an improved understanding of
the influence of the ageostrophic flow on eddy trapping.

5 The value of an RCLV atlas

The biogeochemical applications of SLA eddy atlases frequently relate to the evaluation and interpretation of microbial communities, primary productivity, and carbon export. Such interpretation often hinges on the assumption that most SLA eddies are nonlinear features that trap and transport fluid over conceivably large, lateral distances (Chelton et al., 2011b, a). Under the assumption of coherency, the development of biogeochemical properties of SLA eddy interiors could be interpreted in a simple, Lagrangian frame. However, clouding such presumptions, our analysis shows definitively that approximately half of the SLA-identified features in the NPSG are not coherent from a Lagrangian perspective. Furthermore, for the eddies that do contain a coherent structure, SLA-derived boundaries encompass large areas that do not delineate between dispersive and coherent zones. By identifying RCLV boundaries and capturing their evolution, we can exploit natural perturbation experiments with which to interpret system dynamics: the most coherent mesoscale features can appropriately be considered temporarily "closed" Lagrangian systems.

In summary, we presented a publicly available RCLV atlas (2000-2019) characterizing the natural history of Lagrangian coherent eddy boundaries in the NPSG. Taking advantage of the time-synchronization to remotely sensed ocean color products, high temporal resolution, and backward-in-time coherency of this atlas, the impact of mesoscale eddy trapping on the local biogeochemistry can be addressed. The atlas can be employed in retrospective analysis of observational datasets (e.g., Barone et al., 2019; Rii et al., 2022) and numerous biogeochemical expeditions in the region that targeted mesoscale features (e.g., Seki et al., 2001; Vaillancourt et al., 2003; Benitez-Nelson et al., 2007; Benitez-Nelson and McGillicuddy Jr, 2008; Harke et al., 2021; Zhang et al., 2021; Barone et al., 2022). Additionally, the RCLV atlas is a contextual tool that may aid in future cruise planning and in situ eddy sampling. The applications of this dataset are not limited to biogeochemical applications, as it may also be useful for studies of the dynamical transport of marine plastics, pollution, and heat.

6 Code and data availability

This study was conducted using E.U. Copernicus Marine Service Information, namely the $1/4°$ SLA and geostrophic velocity gridded global ocean dataset (Version 008_047), distributed at https://doi.org/10.48670/moi-00148. Daily and 8-day average chl-a is produced by OC-CCI (Version 6.0 used here) and distributed by the European Space Agency at https://www.oceancolour.org/ (Sathyendranath et al., 2019). The OceanEddies MATLAB software that detects and tracks Eulerian SLA eddy contours is available at https://github.com/ifrenger/OceanEddies (Faghmous et al., 2015). The OceanParcels v2.0 Python package used to run Lagrangian particle simulations is available at https://oceanparcels.org/index.html (Delandmeter and van Sebille, 2019). The floater Python package available at https://github.com/ocean-transport/floater is used to identify RCLV contours and determine their CD. All figures were created with Matplotlib 3.3.4 (Caswell et al., 2021; Hunter, 2007), available under the Matplotlib license at https://matplotlib.org/. GEBCO 2023 bathymetric data were obtained from https://download.gebco.net/.

The Python software developed for this study is available at https://github.com/lexi-jones/RCLVatlas (Jones-Kellett, 2023b). The code includes a pipeline to run OceanParcels on CMEMS data, a custom kernel to calculate the relative vorticity along par-

ticle trajectories, and an RCLV tracking algorithm. The Jupyter notebook script https://github.com/lexi-jones/RCLVatlas/blob/main/example_usage.ipynb includes an example usage code for the software. The NPSG RCLV dataset is publicly available and distributed by Simons CMAP at https://simonscmap.com/catalog/datasets/RCLV_atlas (Jones-Kellett, 2023a).

Video supplement. The 2010 eddy field overlaid on the (a) LAVD and (b) SLA.

Video supplement. Chl-*a* near the Hawaiian Islands from 22 Mar - 01 Nov 2010, highlighting the evolution of a Hawaiian Lee cyclone. The solid contours represent the RCLV and the dashed represents the SLA eddy.

Appendix A: Okubo-Weiss Parameter

The Okubo-Weiss (OW) Parameter is a measure of deformation and rotation defined

$$OW = S_n^2 + S_s^2 - \omega^2 \tag{A1}$$

where S_n is the strain normal to the flow, S_s is the shear strain, ω is the relative vorticity (Okubo, 1970; Weiss, 1991). These are expressed as

$$S_n = \frac{\partial u}{\partial x} - \frac{\partial v}{\partial y}, S_s = \frac{\partial v}{\partial x} + \frac{\partial u}{\partial y}, \omega = \frac{\partial v}{\partial x} - \frac{\partial u}{\partial y} \tag{A2}$$

The OW parameter is sometimes used to identify eddies from satellite geostrophic velocity by detecting circular regions of the flow that switch from strain-dominated to vorticity-dominated.

In Fig. A1, the blue regions are vorticity-dominated ($OW < 0$) and the red are strain-dominated ($OW > 0$). Every RCLV in Fig. A1 encompasses a region of negative OW because both metrics are functions of the relative vorticity. On the other hand, not every low-magnitude OW patch corresponds with an RCLV. The OW parameter is an Eulerian measurement, so it does not detect variations in vorticity in features through time. The OW method is observer-dependent and therefore not sufficient as a standalone metric to determine coherent features of the flow (Haller, 2015). Beron-Vera et al. (2019) shows that the material inside of eddy boundaries derived using the OW method can be more dispersive over time than from boundaries derived from the SLA.
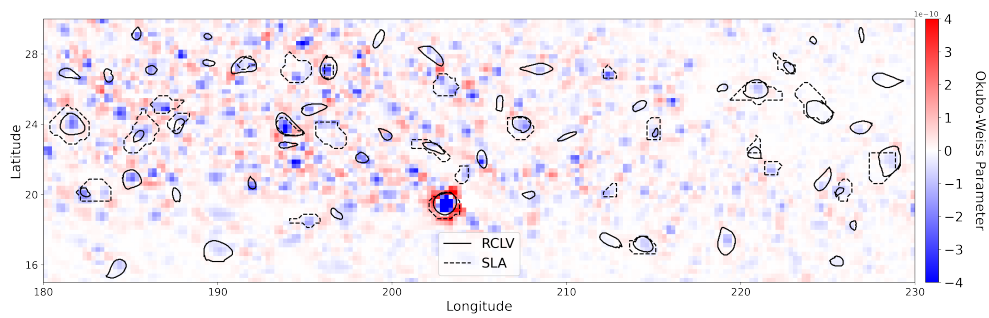
Figure A1. The Okubo-Weiss parameter from 2010 April 23 with RCLV contours (solid lines) and SLA eddy boundaries (dashed lines) plotted on top.
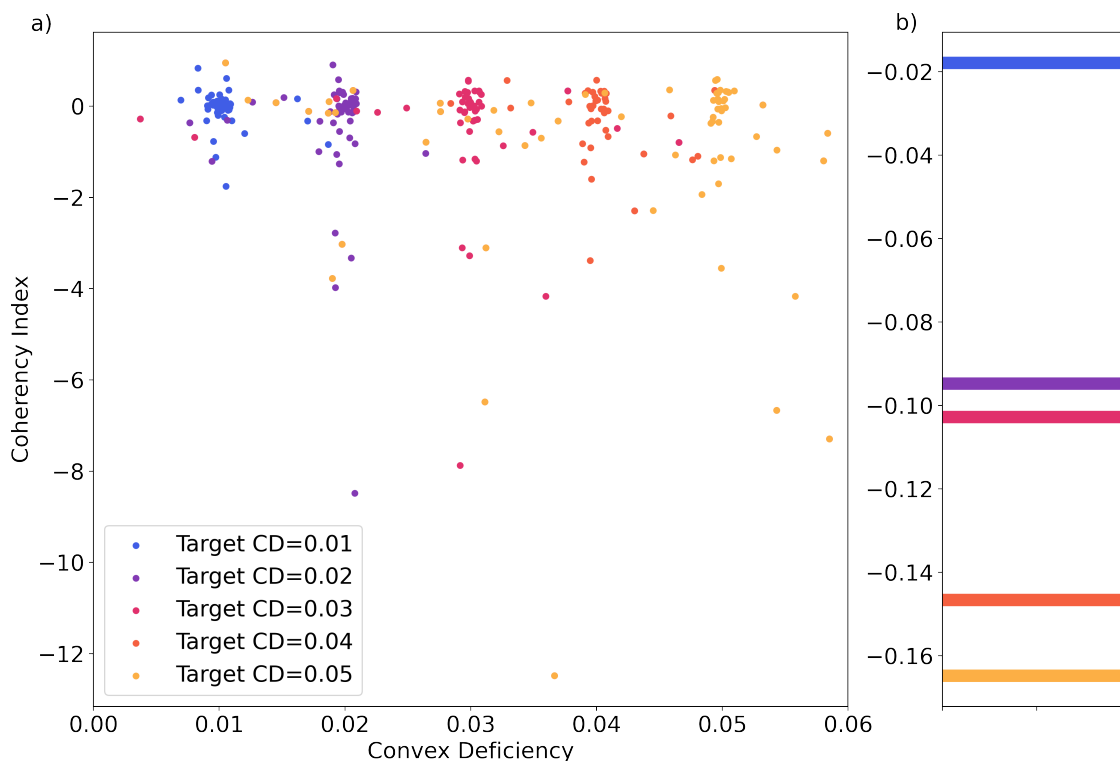
Figure B1. Coherency metrics of RCLV contours on 23 April 2010. (a) CI as a function of CD for various target CDs. (b) Median CI for each target CD.

Appendix B: Coherency Index and Convex Deficiency

490 The result of testing the *floater* algorithm on one day is shown in Appendix Fig. B1. Similar to the results of Tarshish et al. (2018), we find that the median CI decreases as the target CD increases. One might then assume that features with a higher CD tend to be more dispersive, but this is not always the case. There can be a huge spread of CI values from contours identified with any given target CD. For our purposes, a target CD or cutoff is not sufficient as a stand-alone metric to identify features that are coherent. To address this problem, our algorithm iterates through three potential target CDs (0.03, 0.02, 0.01). Starting with

495 target $CD = 0.03$, the CI is calculated for the corresponding contour by tracking all interior Lagrangian particles backward in time for 32 days from the same trajectory data used to produce the LAVD fields. If $CI >= -0.5$ and the sign of the vorticity for 85% of the particles is consistent from day 0 to day -32, then the contour is accepted as an RCLV. Otherwise, the algorithm iterates through the remaining target CDs. In some cases, no contours will qualify at any of the target CDs.
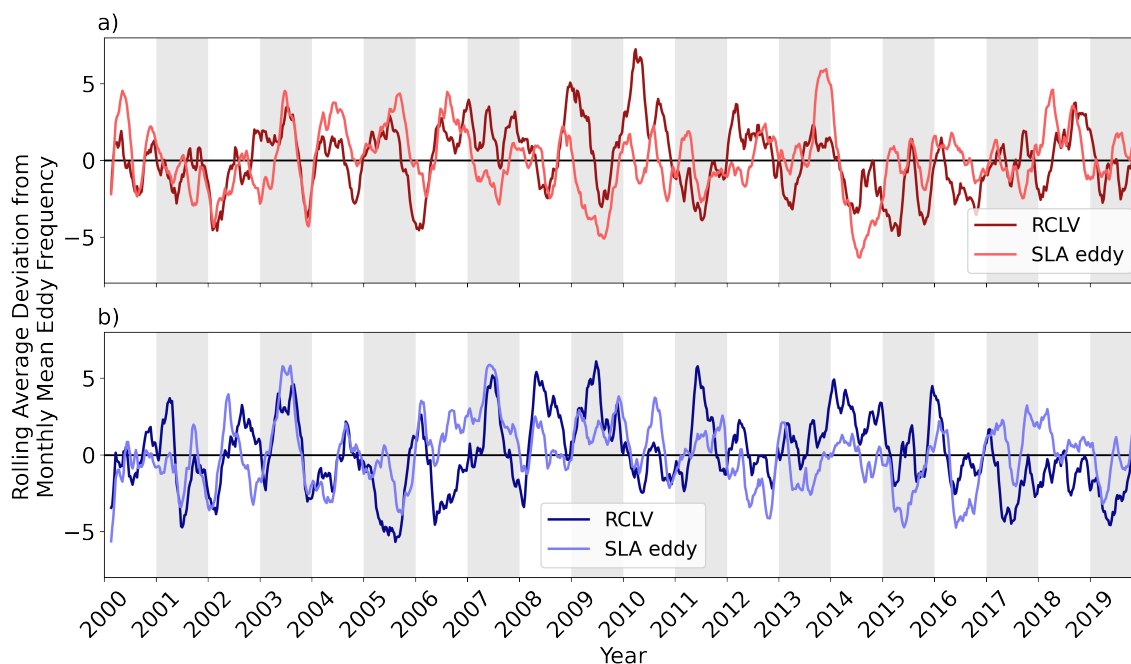
Figure C1. Interannual variability of the number of eddies. (a) Rolling mean daily deviation of the anticyclone frequency from the 2000-2019 monthly mean. (b) Same as (a) but for cyclones.

Table C1. Monthly mean eddy frequency from 2000-2019

	Jan	Feb	Mar	Apr	May	Jun	Jul	Aug	Sep	Oct	Nov	Dec
All RCLVs	36.76	39.04	42.59	47.09	48.69	50.43	50.74	48.29	45.91	42.40	40.53	37.94
RCLV Anti	16.59	18.04	18.43	20.94	21.19	22.69	22.24	20.95	20.60	19.58	18.80	17.56
RCLV Cyc	20.18	21.00	24.16	26.15	27.51	27.74	28.50	27.34	25.31	22.82	21.73	20.34
All SLAs	23.83	26.93	29.46	30.38	33.51	37.45	38.53	35.90	32.11	29.35	27.44	26.14
SLA Anti	10.38	12.50	13.70	14.66	16.08	17.71	17.80	17.23	15.51	14.29	12.43	12.36
SLA Cyc	13.46	14.43	15.76	15.72	17.43	19.74	20.73	18.68	16.60	15.06	15.01	13.78

Appendix C: Temporal Variability
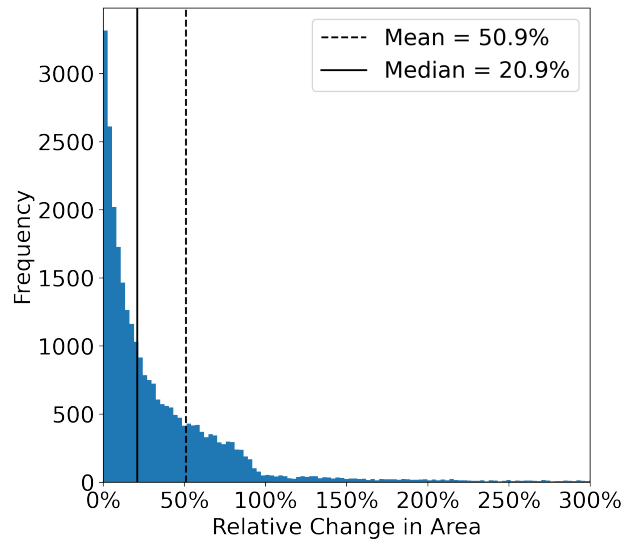
Figure D1. Distribution of the absolute value of the relative change in area between 8-day timesteps for RCLVs that live longer than the minimum 32 days (N = 7059).

500 **Appendix D: Eddy area**
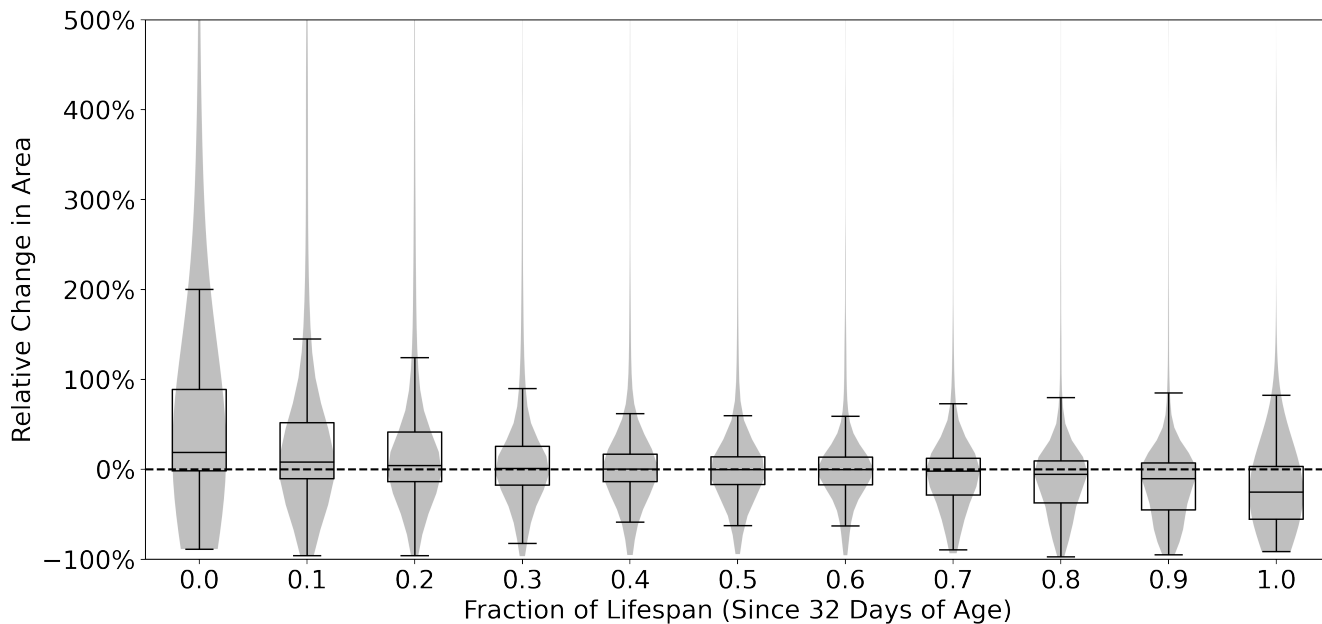
Figure D2. Relative change in area between 8-day timesteps by the fraction of the RCLV lifespan since "birth" at day 32. This only includes RCLVs that live at least 48 days (N = 4962), or three timesteps. The probability distributions are shown in gray by the violin plots and the corresponding box plots are in black. For the box plots, the middle line represents the median, the box spreads the interquartile range, and the whiskers extend to 1.5 times the interquartile range.
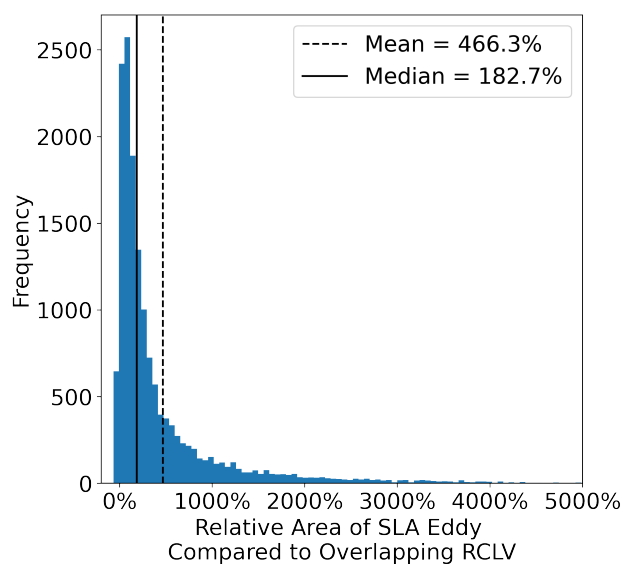
Figure D3. Distribution of the relative difference in area between overlapping SLA eddies and RCLVs (N = 15568).
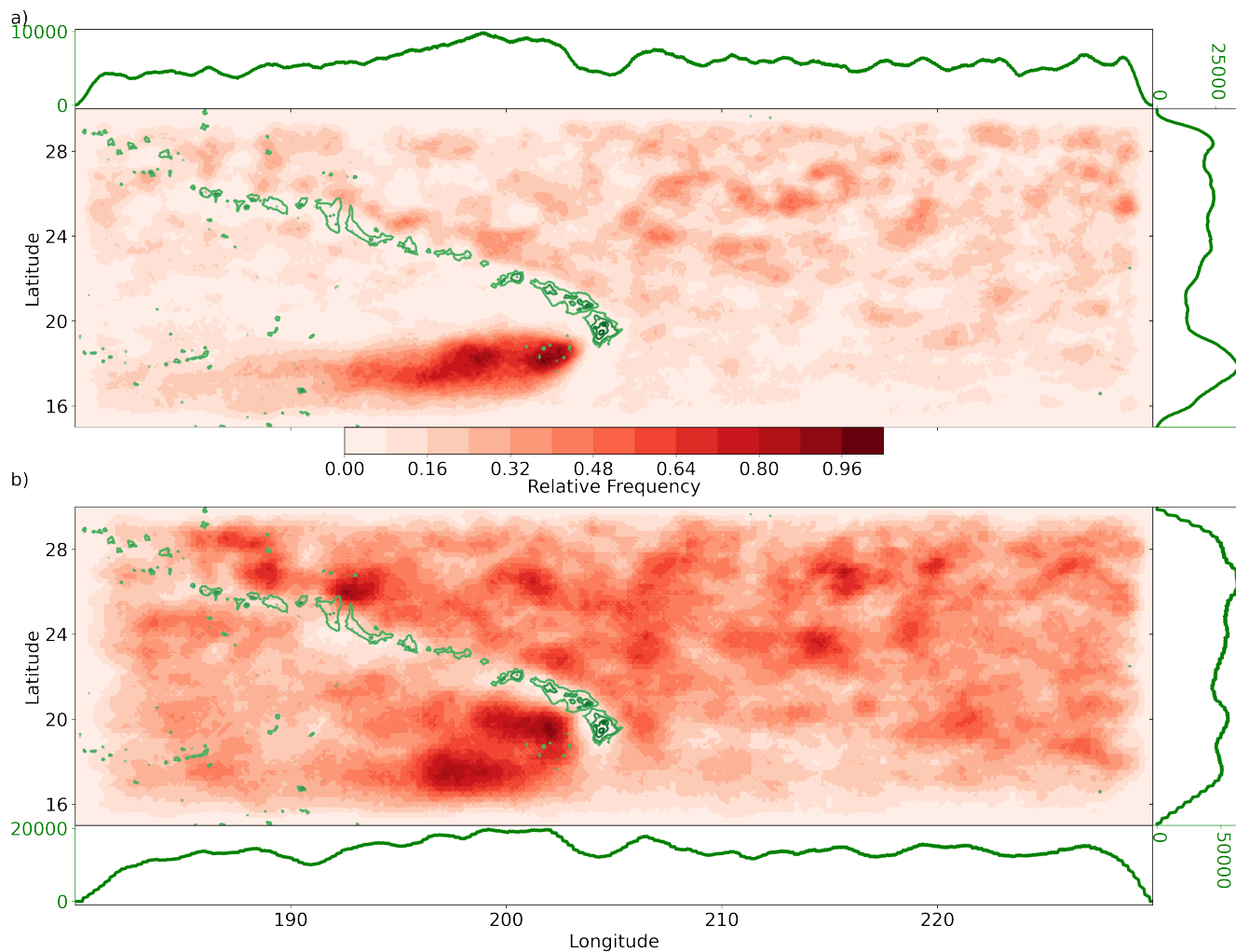
Figure E1. Geographic distribution from 2000-2019 of anticyclonic (a) RCLVs and (b) SLA eddies. The green line plots along the horizontal (vertical) represents the number of times an eddy was present at that longitude (latitude). Frequencies include all coordinate points contained within eddy boundaries. The overlaid green contours show the bathymetry (GEBCO, 2023) above 2000 m below sea level, including the Hawaiian islands and underwater seamounts.

Appendix E: Spatial distributions
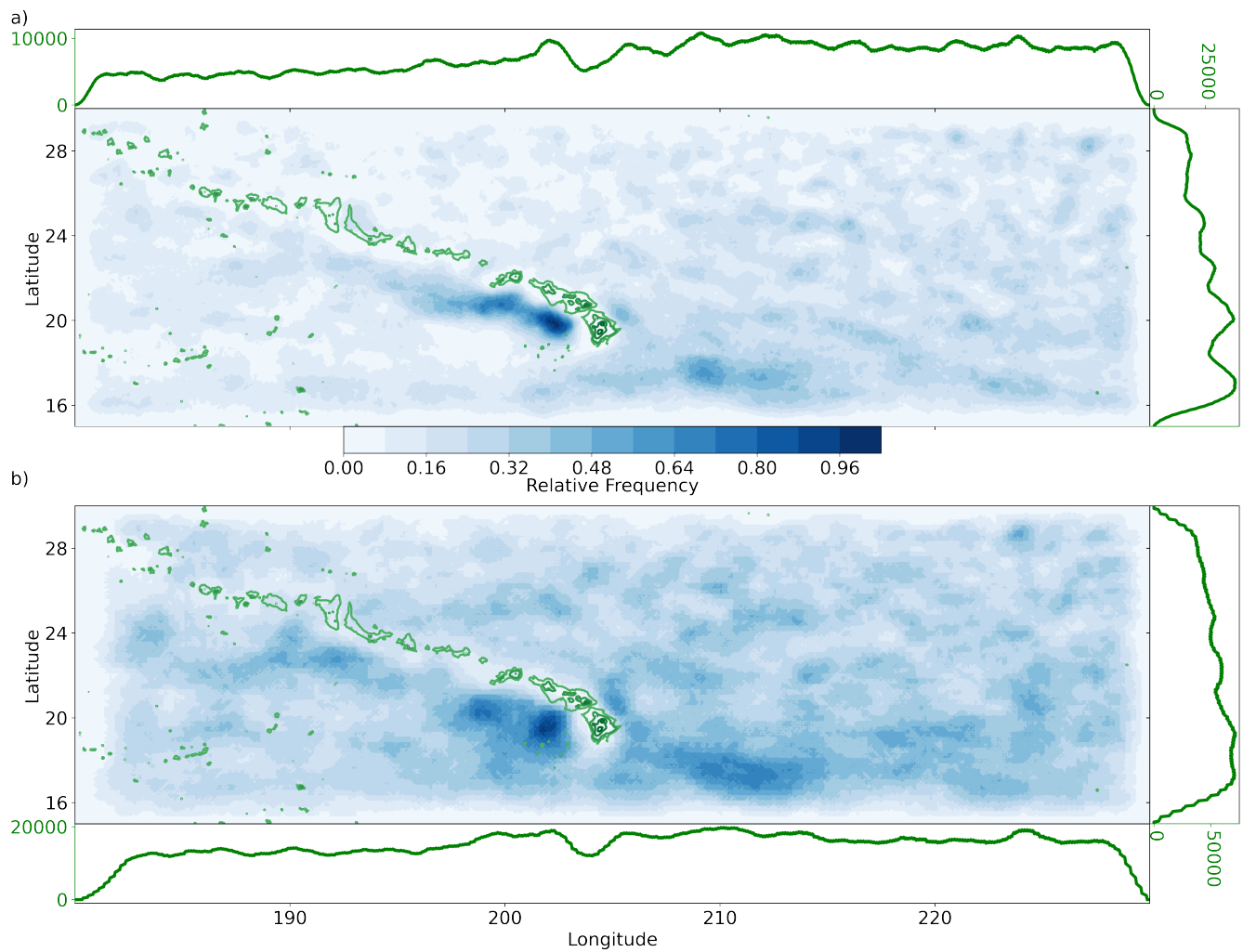
Figure E2. Same as Fig. E1 but for cyclonic (a) RCLVs and (b) SLA eddies.
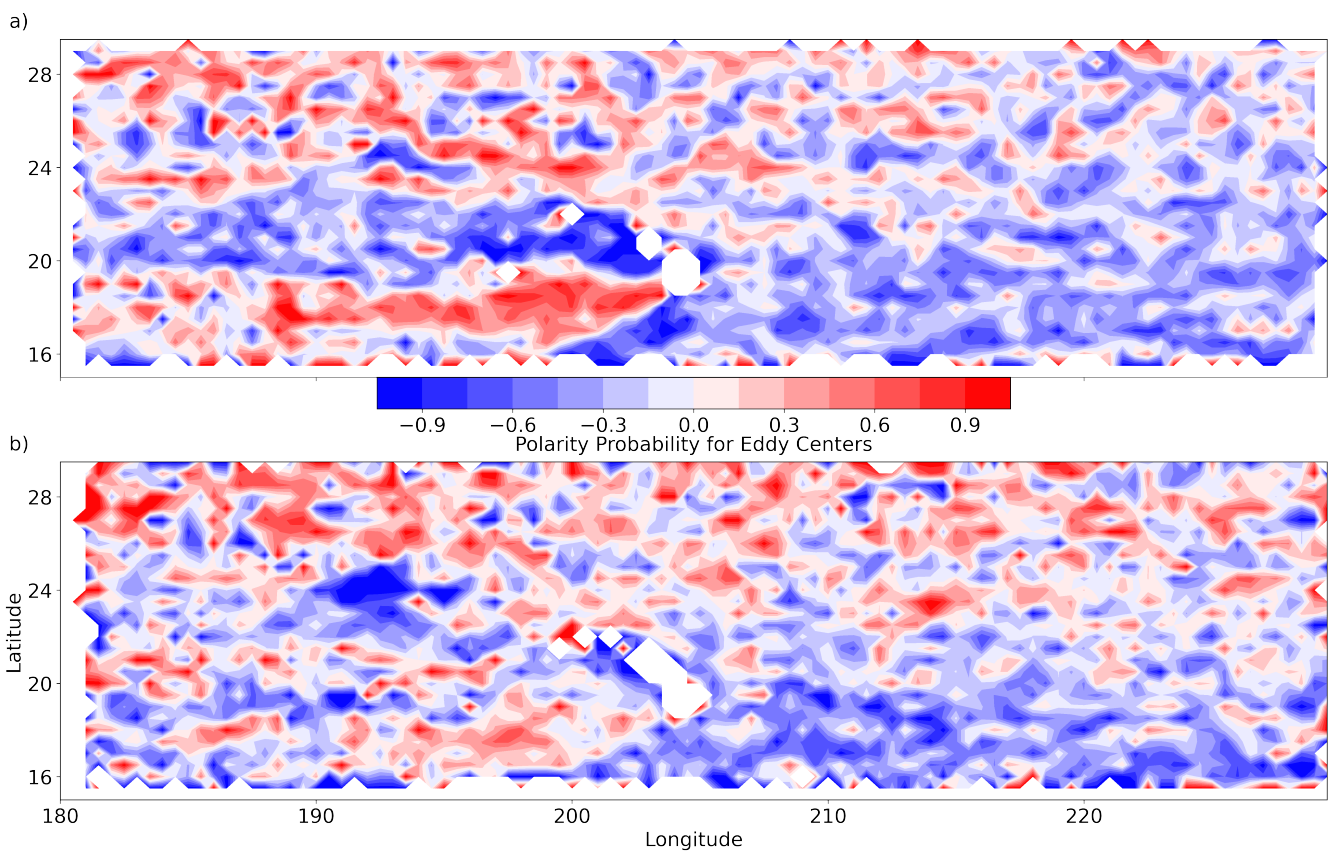
Figure E3. Polarity probability of eddy centers from 2000-2019 for (a) RCLVs and (b) SLA eddies. $P < 0$ (blue) indicates more cyclonic activity, and $P > 0$ (red) more anticyclonic activity.
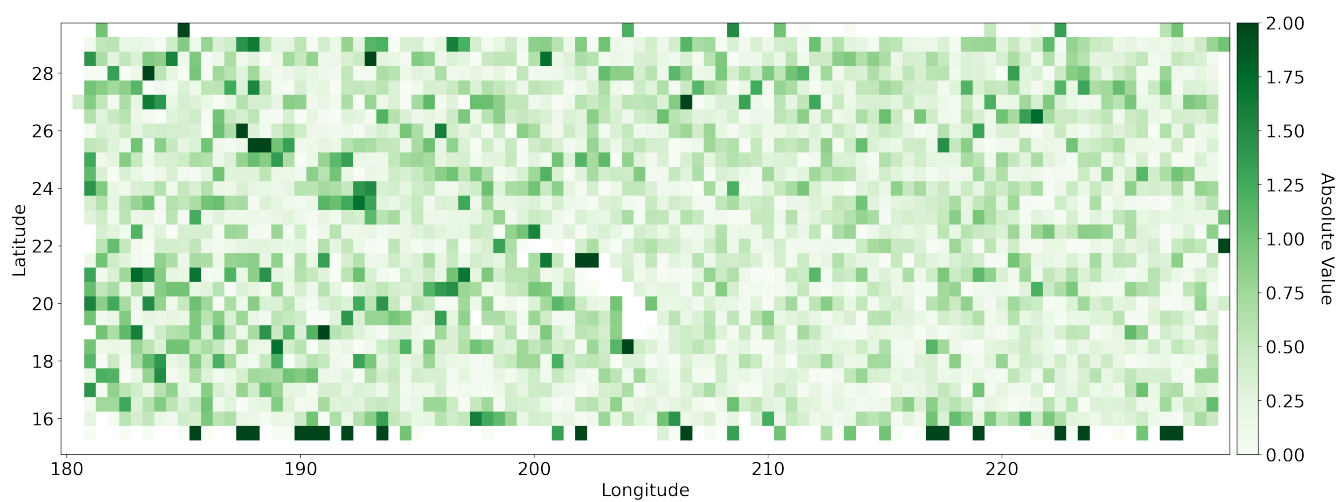
Figure E4. Absolute value of the difference in polarity probability of eddy centers between the RCLV (Fig. E3(a) and SLA eddy atlases (Fig. E3(b)).

Author contributions. The project conceptualization and methodology were developed by all co-authors. AEJK wrote the software, curated the dataset, produced the figures, and conducted the formal analysis, investigation, and validation. AEJK wrote and prepared the manuscript with significant contributions from MJF. MJF acquired funding and resources for the execution of the project.

505   *Competing interests.* The authors declare that they have no conflict of interest.

Acknowledgements. We thank Stephanie Dutkiewicz, Enrico Ser-Giacomi, Stephanie Anderson, Christopher Hill, Gael Forget, and Danling Ma for their invaluable discussions on Lagrangian methodologies and applications. Stephanie Dutkiewicz and Enrico Ser-Giacomi provided helpful feedback that improved this manuscript. We are grateful for support from the Simons Foundation (Simons Collaboration on Ocean Processes and Ecology, Award 329108, M.J.F.; CBIOMES, Award 549931, M.J.F.).

References

Abernathey, R. and Haller, G.: Transport by Lagrangian Vortices in the Eastern Pacific, Journal of Physical Oceanography, 48, 667–685, https://doi.org/10.1175/JPO-D-17-0102.1, 2018.

Andrade-Canto, F., Karrasch, D., and Beron-Vera, F.: Genesis, evolution, and apocalypse of Loop Current rings, Physics of Fluids, 32, https://doi.org/10.1063/5.0030094, 2020.

Andrade-Canto, F., Beron-Vera, F., Goni, G., Karrasch, D., Olascoaga, M., and Triñanes, J.: Carriers of *Sargassum* and mechanism for coastal inundation in the Caribbean Sea, Physics of Fluids, 34, https://doi.org/10.1063/5.0079055, 2022.

Artale, V., Boffetta, G., Celani, A., Cencini, M., and Vulpiani, A.: Dispersion of passive tracers in closed basins: Beyond the diffusion coefficient, Physics of Fluids, 9, https://doi.org/10.1063/1.869433, 1997.

Aurell, E., Boffetta, G., Crisanti, A., Paladin, G., and Vulpiani, A.: Predictability in the large: an extension of the concept of Lyapunov exponent, Journal of Physics A: Mathematical and General, 30, https://doi.org/10.1088/0305-4470/30/1/003, 1997.

Barone, B., Coenen, A., Beckett, S., McGillicuddy, Jr., D., Weitz, J., and Karl, D.: The ecological and biogeochemical state of the North Pacific Subtropical Gyre is linked to sea surface height, Journal of Marine Research, 77, 215–245, https://doi.org/10.1357/002224019828474241, 2019.

Barone, B., Church, M., Dugenne, M., Hawco, N., Jahn, O., White, A., John, S., Follows, M., DeLong, E., and Karl, D.: Biogeochemical Dynamics in Adjacent Mesoscale Eddies of Opposite Polarity, Global Biogeochemical Cycles, 36, https://doi.org/10.1029/2021GB007115, 2022.

Benitez-Nelson, C. and McGillicuddy Jr, D.: Mesoscale physical–biological–biogeochemical linkages in the open ocean: An introduction to the results of the E-Flux and EDDIES programs, Deep Sea Research Part II: Topical Studies in Oceanography, 55, 1133–1138, https://doi.org/10.1016/j.dsr2.2008.03.001, 2008.

Benitez-Nelson, C., Bidigare, R., Dickey, T., Landry, M., Leonard, C., Brown, S., Nencioli, F., Rii, Y., Maiti, K., Becker, J., Bibby, T., Black, W., Cai, W.-J., Carlson, C., Chen, F., Kuwahara, V., Mahaffey, C., McAndrew, P., Quay, P., Rappé, M., Selph, K., Simmons, M., and Yang, E.: Mesoscale Eddies Drive Increased Silica Export in the Subtropical Pacific Ocean, Science, 316, 1017–1021, https://doi.org/10.1126/science.1136221, 2007.

Beron-Vera, F., Wang, Y., Olascoaga, M., Goni, G., and Haller, G.: Objective Detection of Oceanic Eddies and the Agulhas Leakage, Journal of Physical Oceanography, 43, 1426–1438, https://doi.org/10.1175/JPO-D-12-0171.1, 2013.

Beron-Vera, F., Hadjighasem, A., Xia, Q., Olascoaga, M., and Haller, G.: Coherent Lagrangian swirls among submesoscale motions, PNAS, 116, 18 251–18 256, https://doi.org/10.1073/pnas.1701392115, 2019.

Calil, P. and Richards, K.: Transient upwelling hot spots in the oligotrophic North Pacific, Journal of Geophysical Research, 115, https://doi.org/10.1029/2009JC005360, 2010.

Calil, P., Richards, K., Jia, Y., and Bidigare, R.: Eddy activity in the lee of the Hawaiian Islands, Deep-Sea Research II, 55, 1179–1194, https://doi.org/10.1016/j.dsr2.2008.01.008, 2008.

Caswell, T., Droettboom, M., Lee, A., Sales de Andrade, E., Hunter, J., Firing, E., and et al.: Matplotlib v3.3.4, https://doi.org/10.5281/zenodo.4475376, 2021.

Chaigneau, A., Eldin, G., and Dewitte, B.: Eddy activity in the four major upwelling systems from satellite altimetry (1992-2007), Progress in Oceanography, 83, 117–123, https://doi.org/10.1016/j.pocean.2009.07.012, 2009.

Chelton, D., DeSzoeke, R., Schlax, M., El Naggar, K., and Siwertz, N.: Geographic Variability of the First Baroclinic Rossby Radius of Deformation, Journal of Physical Oceanography, 28, 433–460, https://doi.org/10.1175/1520-0485(1998)028<0433:GVOTFB>2.0.CO;2, 1998.

Chelton, D., Schlax, M., Samelson, R., and de Szoeke, R.: Global Observations of large oceanic eddies, Geophysical Research Letters, 34, https://doi.org/10.1029/2007GL030812, 2007.

Chelton, D., Gaube, P., Schlax, M., Early, J., and Samelson, R.: The Influence of Nonlinear Mesoscale Eddies on Near-Surface Oceanic Chlorophyll, Science, 334, 328–332, https://doi.org/10.1126/science.1208897, 2011a.

Chelton, D., Schlax, M., and Samelson, R.: Global observations of nonlinear mesoscale eddies, Progress in Oceanography, 91, 167–216, https://doi.org/10.1016/j.pocean.2011.01.002, 2011b.

Chen, S. and Qiu, B.: Mesoscale eddies northeast of the Hawaiian archipelago from satellite altimeter observations, Journal of Geophysical Research, 115, https://doi.org/10.1029/2009JC005698, 2010.

Dawson, H., Strutton, P., and Gaube, P.: The Unusual Surface Chlorophyll Signatures of Southern Ocean Eddies, Journal of Geophysical Research: Oceans, 123, 6053–6069, https://doi.org/10.1029/2017JC013628, 2018.

Delandmeter, P. and van Sebille, E.: The Parcels v2.0 Lagrangian framework: new field interpolation schemes, Geoscientific Model Development, 12, 3571–3584, https://doi.org/10.5194/gmd-12-3571-2019, 2019.

Denes, M., Froyland, G., and Keating, S.: Persistence and material coherence of a mesoscale ocean eddy, Physical Review Fluids, 7, https://doi.org/10.1103/PhysRevFluids.7.034501, 2022.

Dong, C., Liu, L., Nencioli, F., Bethel, B., Liu, Y., Xu, G., Ma, J., Ji, J., Sun, W., Shan, H., Lin, X., and Zou, B.: The near-global ocean mesoscale eddy atmospheric-oceanic-biological interaction observational dataset, Scientific Data, 9, https://doi.org/10.1038/s41597-022-01550-9, 2022.

Encinas-Bartos, A., Aksamit, N., and Haller, G.: Quasi-objective eddy visualization from sparse drifter data, Chaos, 32, https://doi.org/10.1063/5.0099859, 2022.

Faghmous, J., Frenger, I., Yao, Y., Warmka, R., Lindell, A., and Kumar, V.: A daily global mesoscale ocean eddy dataset from satellite altimetry, Scientific Data, 2, https://doi.org/10.1038/sdata.2015.28, 2015.

Falkowski, P., Ziemann, D., Kolber, Z., and Bienfang, P.: Role of eddy pumping in enhancing primary production in the ocean, Nature, 352, https://doi.org/10.1038/352055a0, 1991.

Ferrari, R. and Wunsch, C.: Ocean Circulation Kinetic Energy: Reservoirs, Sources, and Sinks, Annual Review of Fluid Mechanics, 41, 253–282, https://doi.org/10.1146/annurev.fluid.40.111406.10213, 2009.

Flierl, G. R.: Particle motions in large-amplitude wave fields, Geophysical Astrophysical Fluid Dynamics, 18, 39–74, https://doi.org/10.1080/03091928108208773, 1981.

Frenger, I., Münnich, M., and Gruber, N.: Imprint of Southern Ocean mesoscale eddies on chlorophyll, Biogeosciences, 15, 4781–4798, https://doi.org/10.5194/bg-15-4781-2018, 2018.

Gaube, P., Chelton, D., Strutton, P., and Beherenfeld, M.: Satellite observations of chlorophyll, phytoplankton biomass, and Ekman pumping in nonlinear mesoscale eddies, Journal of Geophysical Research: Oceans, 118, 6349–6370, https://doi.org/10.1002/2013JC009027, 2013.

Gaube, P., McGillicuddy Jr, D., Chelton, D., Behrenfeld, M., and Strutton, P.: Regional variations in the influence of mesoscale eddies on near-surface chlorophyll, Journal of Geophysical Research: Oceans, 119, 8195–8220, https://doi.org/10.1002/2014JC010111, 2014.

Glover, D., Wroblewski, J. S., and McClain, C.: Dynamics of the transition zone in coastal zone color scanner-sensed ocean color in the North Pacific during oceanographic spring, Journal of Geophysical Research: Oceans, 99, 7501–7511, https://doi.org/10.1029/93JC02144, 1994.

Gower, J., Denman, K., and Holyer, R.: Phytoplankton patchiness indicates the fluctuation spectrum of mesoscale oceanic structure, Nature, 288, https://doi.org/10.1038/288157a0, 1980.

Guidi, L., Calil, P., Duhamel, S., Björkman, K., Doney, S., Jackson, G., Li, B., Church, M., Tozzi, S., Kolber, Z., Richards, K., Fong, A., Letelier, R., Gorsky, G., Stemmann, L., and Karl, D.: Does eddy-eddy interaction control surface phytoplankton distribution and carbon export in the North Pacific Subtropical Gyre?, Journal of Geophysical Research, 117, https://doi.org/10.1029/2012JG001984, 2012.

Guo, M., Xiu, P., Li, S., Chai, F., Xue, H., Zhou, K., and Dai, M.: Seasonal variability and mechanisms regulating chlorophyll distribution in mesoscale eddies in the South China Sea, Journal of Geophysical Research: Oceans, 122, 5329–5347, https://doi.org/10.1002/2016JC012670, 2017.

Guo, Y., Bishop, S., Bryan, F., and Bachman, S.: A Global Diagnosis of Eddy Potential Energy Budget in an Eddy-Permitting Ocean Model, Journal of Physical Oceanography, 52, 1731–1748, https://doi.org/10.1175/JPO-D-22-0029.1, 2022.

Haller, G.: Lagrangian Coherent Structures, Annual Review of Fluid Mechanics, 47, 137–162, https://doi.org/10.1146/annurev-fluid-010313-14132, 2015.

Haller, G., Hadjighasem, A., Farazmand, M., and Huhn, F.: Defining coherent vortices objectively from the vorticity, Journal of Fluid Mechanics, 795, 136–173, https://doi.org/10.1017/jfm.2016.151, 2016.

Harke, M., Frischkorn, K., Hennon, G., Haley, S., Barone, B., Karl, D., and Dyhrman, S.: Microbial community transcriptional patterns vary in response to mesoscale forcing in the North Pacific Subtropical Gyre, Environmental Microbiology, 23, 4807–4822, https://doi.org/10.1111/1462-2920.15677, 2021.

He, Q., Tian, F., Yang, X., and Chen, G.: Lagrangian eddies in the Northwestern Pacific Ocean, Journal of Oceanology and Limnology, 40, 66–77, https://doi.org/10.1007/s00343-021-0392-7, 2022.

Hernández-Carrasco, I., Rossi, V., Navarro, G., Turiel, A., Bracco, A., and Orfila, A.: Flow Structures With High Lagrangian Coherence Rate Promote Diatom Blooms in Oligotrophic Waters, Geophysical Research Letters, 50, https://doi.org/10.1029/2023GL103688, 2023.

Hunter, J. D.: Matplotlib: A 2D graphics environment, Computing in Science & Engineering, 9, 90–95, https://doi.org/10.1109/MCSE.2007.55, 2007.

Isern-Fontanet, J., García-Ladona, E., and Font, J.: Identification of Marine Eddies from Altimetric Maps, Journal of Atmospheric and Oceanic Technology, 20, 772–778, https://doi.org/10.1175/1520-0426(2003)20<772:IOMEFA>2.0.CO;2, 2003.

Jones-Kellett, A.: North Pacific Subtropical Gyre RCLV Atlas, https://doi.org/10.5281/zenodo.8139149, 2023a.

Jones-Kellett, A.: RCLVatlas, https://doi.org/10.5281/zenodo.7702978, 2023b.

Karl, D. and Church, M.: Station ALOHA: A Gathering Place for Discovery, Education, and Scientific Collaboration, Limnology and Oceanography Bulletin, 28, 10–12, https://doi.org/10.1002/lob.10285, 2019.

Katsanoulis, S., Farazmand, M., Serra, M., and Haller, G.: Vortex boundaries as barriers to diffusive vorticity transport in two-dimensional flows, Physical Review Fluids, 5, https://doi.org/10.1103/PhysRevFluids.5.024701 I., 2020.

Lehahn, Y., d'Ovidio, F., Lévy, M., Amitai, Y., and Heifetz, E.: Long range transport of a quasi isolated chlorophyll patch by an Agulhas ring, Geophysical Research Letters, 38, https://doi.org/10.1029/2011GL048588, 2011.

Lehahn, Y., Koren, I., Schatz, D., Frada, M., Sheyn, U., Boss, E., Efrati, S., Rudich, Y., Trainic, M., Sharoni, S., Laber, C., DiTullio, G., Coolen, M., Martins, A., Van Mooy, B., Bidle, K., and Vardi, A.: Decoupling Physical from Biological Processes to Assess the Impact of Viruses on a Mesoscale Algal Bloom, Current Biology, 24, 2041–2046, https://doi.org/10.1016/j.cub.2014.07.046, 2014.

Lévy, M., Franks, P., and Smith, K.: The role of submesoscale currents in structuring marine ecosystems, Nature Communications, 9, https://doi.org/10.1038/s41467-018-07059-3, 2018.

Liu, T. and Abernathey, R.: A global Lagrangian eddy dataset based on satellite altimetry, Earth System Science Data, 15, https://doi.org/10.5194/essd-15-1765-2023, 2023.

Liu, T., Abernathey, R., Sinha, A., and Chen, D.: Quantifying Eulerian Eddy Leakiness in an Idealized Model, Journal of Geophysical
625   Research: Oceans, 124, 8869–8886, https://doi.org/10.1029/2019JC015576, 2019.

Liu, T., He, Y., Zhai, X., and Liu, X.: Diagnostics of Coherent Eddy Transport in the South China Sea Based on Satellite Observations,
Remote Sensing, 14, https://doi.org/10.3390/rs14071690, 2022.

Liu, Y., Dong, C., Guan, Y., Chen, D., McWilliams, J., and Nencioli, F.: Eddy analysis in the subtropical zonal band of the North Pacific
Ocean, Deep-Sea Research I, 68, 54–67, https://doi.org/10.1016/j.dsr.2012.06.001, 2012.

630   Liu, Y., Wilson, C., Green, M., and Hughes, C.: Gulf Stream Transport and Mixing Processes via Coherent Structure Dynamics, Journal of
Geophysical Research: Oceans, 123, 3014–3037, https://doi.org/10.1002/2017JC013390, 2018.

Liu, Z., Liao, G., Hu, X., and Zhou, B.: Aspect Ratio of Eddies Inferred From Argo Floats and Satellite Altimeter Data in the Ocean, Journal
of Geophysical Research: Oceans, 125, https://doi.org/10.1029/2019JC015555, 2020.

Lumpkin, C.: Eddies and Currents of the Hawaiian Islands, Ph.D. thesis, School of Ocean and Earth Science and Technology, University of
635   Hawaii, Manoa, 1998.

Mahadevan, A.: The Impact of Submesoscale Physics on Primary Productivity of Plankton, Annual Review of Marine Science, 8, 161—-184,
https://doi.org/10.1146/annurev-marine-010814-015912, 2016.

Mason, E., Pascual, A., and McWilliams, J.: A New Sea Surface Height-Based Code for Oceanic Mesoscale Eddy Tracking, Journal of
Atmospheric and Oceanic Technology, 31, 1181–1188, https://doi.org/10.1175/JTECH-D-14-00019.1, 2014.

640   McGillicuddy Jr, D.: Mechanisms of Physical-Biological-Biogeochemical Interaction at the Oceanic Mesoscale, Annual Review of Marine
Science, 8, 125–159, https://doi.org/10.1146/annurev-marine-010814-015606, 2016.

Ntaganou, N., Kourafalou, V., Beron-Vera, F., Olascoaga, M., Le Hénaff, M., and Androulidakis, Y.: Influence of Caribbean eddies on the
Loop current system evolution, Frontiers in Marine Science, 10, https://doi.org/10.3389/fmars.2023.961058, 2023.

Okubo, A.: Horizontal dispersion of floatable particles in the vicinity of velocity singularities such as convergences, Deep-Sea Research, 17,
645   445–454, https://doi.org/10.1016/0011-7471(70)90059-8, 1970.

Pegliasco, C., Delepoulle, A., Mason, E., Morrow, R., Faug`ere, Y., and Dibarboure, G.: META3.1exp: a new global mesoscale eddy trajectory
atlas derived from altimetry, Earth System Sciencew Data, 14, https://doi.org/10.5194/essd-14-1087-2022, 2022.

Pierrehumbert, R. and Yang, H.: Global Chaotic Mixing on Isentropic Surfaces, Journal of the Atmospheric Sciences, 50,
https://doi.org/10.1175/1520-0469(1993)050<2462:GCMOIS>2.0.CO;2, 1992.

650   Rieck, J., Böning, C., Greatbatch, R., and Scheinert, M.: Seasonal variability of eddy kinetic energy in a global high-resolution ocean model,
Geophysical Research Letters, 42, 9379–9386, https://doi.org/10.1002/2015GL066152, 2015.

Rii, Y., Peoples, L., Karl, D., and Church, M.: Seasonality and episodic variation in picoeukaryote diversity and structure re-
veal community resilience to disturbances in the North Pacific Subtropical Gyre, Limnology and Oceanography, 67, S331–S351,
https://doi.org/10.1002/lno.11916, 2022.

655   Rousselet, L., de Verneil, A., Doglioli, A., Petrenko, A., Duhamel, S., Maes, C., and Blanke, B.: Large- to submesoscale surface circula-
tion and its implications on biogeochemical/biological horizontal distributions during the OUTPACE cruise (southwest Pacific), Biogeo-
sciences, 15, 2411–2431, https://doi.org/10.5194/bg-15-2411-2018, 2018.

Sasaki, H., Klein, P., Sasai, Y., and Qiu, B.: Regionality and seasonality of submesoscale and mesoscale turbulence in the North Pacific
Ocean, Ocean Dynamics, 67, 1195–1216, https://doi.org/10.1007/s10236-017-1083-y, 2017.

660 Sasaki, H., Qiu, B., Klein, P., Nonaka, M., and Sasai, Y.: Interannual Variations of Submesoscale Circulations in the Subtropical Northeastern
       Pacific, Geophysical Research Letters, 49, https://doi.org/10.1029/2021GL097664, 2022.

   Sathyendranath, S., Brewin, R., Brockmann, C., Brotas, V., Calton, B., Chuprin, A., Cipollini, P., Couto, A., Dingle, J., Doerffer, R., Donlon,
       C., Dowell, M., Farman, A., Grant, M., Groom, S., Horseman, A., Jackson, T., Krasemann, H., Lavender, S., Martinez-Vicente, V.,
       Mazeran, C., Mélin, F., Moore, T., Mu¨ller, D., Regner, P., Roy, S., Steele, C., Steinmetz, F., Swinton, J., Taberner, M., Thompson, A.,
665   Valente, A., Zu¨hlke, M., Brando, V., Feng, H., Feldman, G., Franz, B., Frouin, R., Gould, Jr., R., Hooker, S., Kahru, M., Kratzer, S.,
       Mitchell, B., Muller-Karger, F., Sosik, H., Voss, K., Werdell, J., and Platt, T.: An ocean-colour time series for use in climate studies: the
       experience of the Ocean-Colour Climate Change Initiative (OC-CCI)., Sensors, 19, https://doi.org/10.3390/s19194285, 2019.

   Schubert, R., Gula, J., Greatbatch, R., Baschek, B., and Biastoch, A.: The Submesoscale Kinetic Energy Cascade: Mesoscale Ab-
       sorption of Submesoscale Mixed Layer Eddies and Frontal Downscale Fluxes, Journal of Physical Oceanography, 50, 2573–2589,
670   https://doi.org/10.1175/JPO-D-19-0311.1, 2020.

   Seki, M., Polovina, J., Brainard, R., Bidigare, R., Leonard, C., and Foley, D.: Biological enhancement at cyclonic eddies tracked with GOES
       thermal imagery in Hawaiian waters, Geophysical Research Letters, 28, 1583–1586, https://doi.org/10.1029/2000GL012439, 2001.

   Sinha, A., Balwada, D., Tarshish, N., and Abernathey, R.: Modulation of Lateral Transport by Submesoscale Flows and Inertia-Gravity
       Waves, Journal of Advances in Modeling Earth Systems, 11, 1039–1065, https://doi.org/10.1029/2018MS001508, 2019.

675 Tarshish, N., Abernathey, R., Zhang, C., Dufour, C., Frenger, I., and Griffies, S.: Identifying Lagrangian coherent vortices in a mesoscale
       ocean model, Ocean Modelling, 130, 15–28, https://doi.org/10.1016/j.ocemod.2018.07.001, 2018.

   Tian, F., Wang, M., Liu, X., He, Q., and Chen, G.: SLA-Based Orthogonal Parallel Detection of Global Rotationally Coherent Lagrangian
       Vortices, Journal of Atmospheric and Oceanic Technology, 39, https://doi.org/10.1175/JTECH-D-21-0103.1, 2022.

   Uchida, T., Abernathey, R., and Smith, S.: Seasonality of eddy kinetic energy in an eddy permitting global climate model, Ocean Modelling,
680   118, 41–58, https://doi.org/10.1016/j.ocemod.2017.08.006, 2017.

   Vaillancourt, R., Marra, J., Seki, M., Parsons, M., and Bidigare, R.: Impact of a cyclonic eddy on phytoplankton community structure and
       photosynthetic competency in the subtropical North Pacific Ocean, Deep-Sea Research I, 50, 829–847, https://doi.org/10.1016/S0967-
       0637(03)00059-1, 2003.

   Villar, E., Farrant, G., Follows, M., Garczarek, L., Speich, S., Audic, S., Bittner, L., Blanke, B., Brum, J., and Iudicone, D.: Environmental
685   characteristics of Agulhas rings affect interocean plankton transport, Science, 348, https://doi.org/10.1126/science.1261447, 2015.

   Vortmeyer-Kley, R., Holtermann, P., Feudel, U., and Gräwe, U.: Comparing Eulerian and Lagrangian eddy census for a tide-less, semi-
       enclosed basin, the Baltic Sea, Ocean Dynamics, 69, 701–717, https://doi.org/10.1007/s10236-019-01269-z, 2019.

   Waite, A., Pesant, S., Griffin, D., Thompson, P., and Holl, C.: Oceanography, primary production and dissolved inorganic nitrogen uptake in
       two Leeuwin Current eddies, Deep-Sea Research II, 54, 981–1002, https://doi.org/10.1016/j.dsr2.2007.03.001, 2007.

690 Wang, Y., Olascoaga, M., and Beron-Vera, F.: Coherent water transport across the South Atlantic, Geophysical Research Letters, 42, 4072–
       4079, https://doi.org/10.1002/2015GL064089, 2015.

   Weiss, J.: The dynamics of enstrophy transfer in two-dimensional hydrodynamics, Physica D, 48, 273–294, https://doi.org/10.1016/0167-
       2789(91)90088-Q, 1991.

   Xia, Q., Dong, C., He, Y., Li, G., and Dong, J.: Lagrangian Study of Several Long-Lived Agulhas Rings, Journal of Physical Oceanography,
695   52, 1049–1072, https://doi.org/10.1175/JPO-D-21-0079.1, 2022a.

   Xia, Q., Li, G., and Dong, C.: Global Oceanic Mass Transport by Coherent Eddies, Journal of Physical Oceanography, 52, 1111–1132,
       https://doi.org/10.1175/JPO-D-21-0103.1, 2022b.

Yoshida, S., Qiu, B., and Hacker, P.: Wind-generated eddy characteristics in the lee of the island of Hawaii, Journal of Geophysical Research, 115, https://doi.org/10.1029/2009JC005417, 2010.

700   Yoshida, S., Qiu, B., and Hacker, P.: Low-frequency eddy modulations in the Hawaiian Lee Countercurrent: Observations and connection to the Pacific Decadal Oscillation, Journal of Geophysical Research, 116, https://doi.org/10.1029/2011JC007286, 2011.

Zhai, X., Greatbatch, R., and Kohlmann, J.: On the seasonal variability of eddy kinetic energy in the Gulf Stream region, Geophysical Research Letters, 35, https://doi.org/10.1029/2008GL036412, 2008.

Zhang, W., Wofe, C., and Abernathey, R.: Role of Surface-Layer Coherent Eddies in Potential Vorticity Transport in Quasigoestrophic

705   Turbulence Driven by Eastward Shear, Fluids, 5, https://doi.org/10.3390/fluids501000, 2020.

Zhang, Y., Ryan, J., Hobson, B., Kieft, B., Romano, A., Barone, B., Preston, C., Roman, B., Raanan, B.-Y., Pargett, D., Dugenne, M., White, A., Henderix Freitas, F., Poulos, S., Wilson, S., Delong, E., Karl, D., Birch, J., Bellingham, J., and Scholin, C.: A system of coordinated autonomous robots for Lagrangian studies of microbes in the oceanic deep chlorophyll maximum, Science Robotics, 6, https://doi.org/10.1126/scirobotics.abb9138, 2021.